國 立 中 央 大 學

大 氣 科 學 學 系 大 氣 物 理 碩 士 班

碩 士 論 文

探討高時間解析度降雨資料

對臺灣淹水模擬之影響：以宜蘭和高雄為例

Investigating the Impact of High Temporal-Resolution Precipitation Data on Flood Simulations in Taiwan: A Case Study of Yilan and Kaohsiung

研 究 生：林 芸 安

指導教授：鍾 高 陞 博 士

中 華 民 國　一 一 四　年　六　月

國立中央大學圖書館學位論文授權書

填單日期：2025 / 07 / 25　　2019.9 版

授權人姓名	林芸安	學 號	112621012
系所名稱	大氣科學學系大氣物理所	學位類別	☑碩士　□博士
論文名稱	探討高時間解析度降雨資料對臺灣淹水模擬之影響：以宜蘭知高程為例	指導教授	鍾高陞

學位論文網路公開授權

授權本人撰寫之學位論文全文電子檔：

- 在「**國立中央大學圖書館博碩士論文系統**」.
  - (√)同意立即網路公開
  - (　)同意 於西元＿＿＿年＿＿＿月＿＿＿日網路公開
  - (　)不同意網路公開，原因是：＿＿＿＿＿＿＿＿＿＿
- 在**國家圖書館「臺灣博碩士論文知識加值系統」**
  - (√)同意立即網路公開
  - (　)同意 於西元＿＿＿年＿＿＿月＿＿＿日網路公開
  - (　)不同意網路公開，原因是：＿＿＿＿＿＿＿＿＿＿

依著作權法規定，非專屬、無償授權國立中央大學、台灣聯合大學系統與國家圖書館，不限地域、時間與次數，以文件、錄影帶、錄音帶、光碟、微縮、數位化或其他方式將上列授權標的基於非營利目的進行重製。

學位論文紙本延後公開申請 (紙本學位論文**立即公開者此欄免填**)

本人撰寫之學位論文紙本因以下原因將延後公開

- **延後原因**
  - (　)已申請專利並檢附證明，專利申請案號：
  - (　)準備以上列論文投稿期刊
  - (　)涉國家機密
  - (　)依法不得提供，請說明：＿＿＿＿＿＿＿＿

- **公開日期**：西元＿＿＿＿＿年＿＿＿＿＿月＿＿＿＿＿日

※繳交教務處註冊組之紙本論文(送繳國家圖書館)若不立即公開，請加填「國家圖書館學位論文延後公開申請書」

研究生簽名：林芸安　　指導教授簽名：鍾高陞

*本授權書請完整填寫並親筆簽名後，裝訂於論文**封面之次頁**。

國立中央大學碩士班研究生
論 文 指 導 教 授 推 薦 書

大氣科學學系大氣物理碩士班 學系/研究所 林芸安 研究生

所提之論文 探討高時間解析度降雨資料對臺灣淹水模擬之影響:以宜蘭和高雄為例

係由本人指導撰述，同意提付審查。

指導教授 鍾高陞 (簽章)

114 年 6 月 2 日

1140611

國立中央大學碩士班研究生
論文口試委員審定書

大氣科學學系大氣物理碩士班 學系/研究所 林芸安 研究生

所提之論文 探討高時間解析度降雨資料對臺灣淹水模擬之影響:以宜蘭和高雄為例

經由委員會審議，認定符合碩士資格標準。

學位考試委員會召集人 楊尊華

委　　員 鍾高陞

莫楷翔

許承欽

中　華　民　國　114　年　6　月　11　日

1140611

摘要

台灣擁有豐沛的降雨，但也有致災的可能性，因此高解析度淹水模擬及預報對防災及水資源管理是重要的，但淹水模擬及預報的準確性有很多誤差來源，包括地形資料的準確度、模型的設定、以及降雨資料的不確定性。

本研究針對降雨資料的不確定性，將不同類型及時間解析度的降雨資料應用至 3Di 水動力模式，包括理想情境下的降雨、定量降水估計、和 MAPLE (McGill Algorithm for Precipitation nowcasting using Lagrangian Extrapolation)的即時預報結果，以此檢視 3Di 模式對降雨資料的敏感度，並選擇宜蘭的冬山河流域及高雄市區，模擬 2024 年發生的多個颱風、東北季風造成的淹水事件，以此檢視不同集水區和降雨型態的差異性。過去臺灣用在水文分析的降雨資料大多都是一小時一筆累積降水資料，但當強降雨集中在更短時間例如半小時或十分鐘時，根據實驗結果，可能造成淹水情形更加嚴重，因此更高時間解析度的降雨資料是有存在的必要性。在即時預報方面，MAPLE 的即時預報在每小時滾動更新的條件下，淹水歷線趨勢上和使用定量降水估計的模擬相似，但整體淹水面積低估。

此外，淹水模式時常因為真實資料不足或零散而難以驗證，但 2024 年的凱米颱風在台灣造成多處淹水而有相對充足的資料，因此本研究利用淹水感測器、衛星資料及 Emergency Management Information Cloud (EMIC) 作為模式驗證的參考，也顯示了不同資料的優缺點及結果上的差異。根據校驗結果，3Di 水動力模式的模擬結果和淹水感測器相比，準確度在不同事件下分布在 0.6 至 0.8，和衛星資料相比，準確度分布在 0.75 和 0.95 之間。

Abstract

The accuracy of flood simulations depends on multiple factors, with precipitation data uncertainty being a key influence. Therefore, selecting an appropriate combination of meteorological data and flood models is essential for effective flood management. This study presents a framework that emphasizes the importance of high-temporal-resolution precipitation data by integrating five types of precipitation datasets: designed rainfall, two quantitative precipitation estimation (QPE) products, and the nowcast system MAPLE (McGill Algorithm for Precipitation Nowcasting using Lagrangian Extrapolation). These datasets were used as inputs for the hydrodynamic model 3Di.

An idealized experiment revealed that flooding may be underestimated when heavy rainfall occurs within a short duration, particularly less than one hour, if only hourly rainfall data is used, underscoring the necessity of finer temporal resolution in flood forecasting. Six heavy rainfall events from 2024 in northeastern and southwestern Taiwan were analyzed, leveraging improved data availability from these events to validate the flood model. The results demonstrate that higher temporal resolution enables earlier flood detection, which is critical for early warning systems. Additionally, when rainfall intensity increases, the discrepancy between flood extents generated by different datasets becomes more pronounced. Furthermore, MAPLE provides reliable short-term forecasts within one hour, though any forecast errors may be amplified when incorporated into the flood model. These findings highlight the importance of precise precipitation data in flood simulations and the potential challenges associated with forecast uncertainty.

Acknowledgment

光陰荏苒，六年在中央的求學時光轉瞬即逝。大三時因緣際會選修了雷達專題課程並參與 TAHOPE 觀測實驗，將課堂所學實際應用於觀測工作，也因此萌生了繼續攻讀研究所的想法。首先，誠摯感謝鍾高陞老師自專題開始，至碩士兩年間的悉心指導。碩士期間我面臨過許多困難與迷惘，老師總是耐心協助我釐清思緒、提供方向建議，也給予我極大的自由與信任，讓我得以自在發揮與學習。同時感謝許永佳博士從大四起一步步帶領我進入水利工程的領域，並讓我實際參與相關工作，進而深入理解水利領域對降雨資料的需求。此外，也感謝廖宇慶老師、張偉裕老師在課堂與研究上的啟發，以及黃椿喜博士與楊尊華老師於論文口試過程中所給予的寶貴建議，讓研究更加完善。在論文收尾之際，很開心可以參與 TEAM-R 觀測實驗以及探空施放，為我的研究生活增添了寶貴的實務體驗。

一路走來，謝謝育蕎學姐從大三專題的協助，至碩士階段都不厭其煩跟我討論，冠維學長從大四教我許多水利相關知識，協助我解決困難，也謝謝大柯學姐、沁全學長、采蓉學姐給我研究的想法和幫助，讓我獲益良多。謝謝雷達實驗室的皓宇、廉翔、倚彤、世楷、琦竣、Ruel，即使大家個性截然不同，仍組成一個獨特又溫暖的團體，為碩士生活增添無數回憶，也謝謝同屆的夥伴互相扶持。另外，謝謝游泳隊的大家讓我在實驗室之外，多了一個轉換心情、調劑身心的地方，使我兩年的生活更加平衡及多彩。最後，最深的感謝給我最愛的父母、弟弟，始終支持我的每一個選擇，讓我能勇敢面對困難、克服挫折，也謝謝世楷一直以來的陪伴，讓我在這段旅程中始終不孤單。

Outline

List of Tables

List of Figures

Chapter 1. Introduction

In Taiwan, the occurrence of extreme rainfall, precipitated by tropical cyclones, frequently results in disastrous flooding. This phenomenon has been associated with significant societal and economic consequences, including injuries, property damage, and economic losses. The topography of Taiwan is characterised by a high degree of slope, a high population density, and rapid urbanisation. These factors combine to amplify the risk of flooding, particularly in low-elevation and coastal regions. Flood management has become increasingly difficult in recent years due to climate change, which has increased both the severity and frequency of extreme weather occurrences. (Zwiers et al. 2013; Trenberth 2010; Lawrence et al. 2013). To mitigate the impacts of flooding, it is crucial to have accurate weather forecasts, real-time hydrological monitoring, and efficient flood management strategies.

Flood forecasting faces many sources of uncertainty, including rainfall input, model structure, model parameters, and terrain characteristics (Papaioannou et al. 2017). Rainfall input serves as the internal forcing for flood models. However, uncertainties in rainfall input remain a major challenge, directly influencing the accuracy of flood forecasts. With advancements in computational techniques and observational technology, numerical weather prediction (NWP) systems have significantly improved in recent years, providing high-resolution rainfall forecasts for flood modeling (Cloke and Pappenberger 2009; Alfieri et al. 2012). However, initial forecasts from numerical weather models are often unreliable due to spin-up issues (Saadi et al. 2023; Hsu, 2023).

To overcome this limitation, quantitative precipitation nowcasts (QPN) provide short-term rainfall predictions with high temporal resolution. One widely used technique is radar extrapolation, which relies on a motion field derived from previous radar echoes. This motion field is then applied using advection or other schemes to generate forecasts. The McGill Algorithm for Precipitation nowcasting by Lagrangian Extrapolation (MAPLE) system is one of the QPN approaches. Previous studies have demonstrated MAPLE's capability in nowcasting precipitation across different regions, including North America, Korea, and Europe (Germann and Zawadzki, 2002; Turner et al., 2004; Germann et al., 2006; Bellon et al., 2010; Lee et al., 2010; Mandapaka et al., 2011). In Taiwan, MAPLE was first applied by Pan et al. (2018) to evaluate its performance during typhoon events and a Mei-Yu event. Their results demonstrated that MAPLE can provide an effective forecast duration of approximately 2 hours. A subsequent study (Chung and Yao 2019) analyzed 16 typhoon cases, providing a statistical assessment of MAPLE's performance at different stages of typhoon progression.

Beyond rainfall accuracy, the spatiotemporal variability of precipitation also introduces considerable uncertainty in flood estimation, particularly in small urban basins. These catchments typically exhibit a rapid hydrological response and are highly sensitive to the distribution of rainfall due to the prevalence of impervious surfaces, such as roads and buildings, which promote rapid runoff and limit infiltration (Emmanuel et al. 2012; Ochoa-Rodriguez et al. 2015). These conditions underscore the need for flood forecasting strategies that account for both the accuracy of rainfall and the localized surface characteristics.

Terrain characteristics further contribute to modeling uncertainty by influencing how surface water is routed and stored. Accurate terrain representation is especially crucial in hydrodynamic simulations. Lai (2022), for example, compared the performance of two hydrodynamic models, 3Di and HEC-RAS, under different return period scenarios in Taiwan. The study found that 3Di provided more realistic and detailed inundation maps, benefiting from quadtree and subgrid techniques that preserve terrain detail while reducing computational load. Similarly, Hsu et al. (2016) demonstrated that the resolution of digital elevation models (DEMs) can significantly affect model performance. Coarser DEMs often oversimplify topographic features, which may distort hydraulic gradients and result in unrealistic flood extents.

Verifying hydrodynamic models is challenging due to limited observational data (Wing et al., 2017). Traditionally, flood model validation relied on surveys and eyewitness reports. However, in recent years, IoT-based flood sensors in Taiwan have provided quantitative measurements of water depth on roads and low-lying areas. Meanwhile, Satellite-based Synthetic Aperture Radar (SAR) sensors are also widely recognized for their effectiveness in flood detection by distinguishing water bodies through their low scatter values. SAR offers the advantage of penetrating cloud cover and providing flood extent at a two-dimensional scale, and it has been successfully used to calibrate hydrodynamic forecast models (Schumann et al., 2009; Grimaldi et al., 2016). However, meteorological and surface features can affect SAR backscatter characteristics, leading to false detection. For example, radar shadow and surface covered by buildings and vegetation may obscure flooded areas (Grimaldi et al. 2016). Many previous studies have relied on a single type of flood observation data, limiting

the ability to comprehensively assess flood conditions.

Flood simulation accuracy is highly sensitive to the temporal resolution and distribution of rainfall input. Traditional models often assume uniform rainfall distribution, which may not accurately represent short-duration, high-intensity events that drive urban flooding. This study aims to investigate the impacts of rainfall time resolution on flood simulation using the 3Di hydrodynamic model and to assess the value of different rainfall input types, including nowcasting and QPE products, in improving prediction accuracy and early warning capabilities.

Idealized rainfall scenarios were first designed to test the model's sensitivity: both with the same one-hour total rainfall but different temporal distributions, one evenly spread and one concentrated in 10 minutes, and one in 30 minutes. The results show that the scenario which the rainfall concentrated in 10 minutes has higher inundation area, indicating the 3Di model is capable of distinguishing between different rainfall distributions, confirming the critical role of rainfall intensity. In real cases, the 3Di model was applied to six real flood events in Taiwan, integrating high-resolution (1-meter) DEMs to capture terrain features and guide overland flow paths with Rainfall inputs included two quantitative precipitation estimation (QPE) products and MAPLE nowcasting data, indicating the higher temporal resolution of QPE can detect flood earlier. Moreover, MAPLE nowcasting capture overall trend in Kaohsiung, while the forecast error, and the higher-sensitivity of smaller basin lead to more discrepancy in Dongshan. These findings highlight the importance of fine-scale rainfall data in operational flood forecasting and early warning systems.

The Model validation employed a combination of witness reports, flood

sensors, and SAR (Synthetic Aperture Radar) imagery, offering both point-based and spatial assessments. In urban areas like Kaohsiung, where observational data are more abundant, the model performed reliably, and SAR imagery further enhanced spatial validation.

This study is organized as follows. Chapter 2 presents the study area and selected cases. Chapter 3 introduces the hydrological models, QPE data, nowcasting system, and the evaluation framework. Chapter 4 introduces the verification data and approaches. Chapter 5 discusses the results of the idealized test, nowcast performance, hydrodynamic model verification, and the hydrological performance of varying precipitation input. Conclusion and future work are covered in Chapter 6.

Chapter 2. Study area and cases overview

2.1 Study area

Two different characteristic regions are selected for the study, one is the Dongshan River basin, located in Yilan, northeastern Taiwan. The area is 112.718km^2, where the average annual precipitation is about 3000 mm. In Yilan County, rainfall is concentrated during the autumn and winter months from August to December. Typhoons and the northeast monsoon often bring heavy rain. Dongshan Township, which is mostly flat, is traversed by the Dongshan River and Luodong River, making it at risk of river flooding and inundation. In the southwestern part of the first study area is relatively elevated, while the northeastern area is flatter. As a result, during heavy rain or typhoons, flooding is more likely to occur in the northeastern region. If this occurs with high tide, it can further hinder the drainage of floodwaters, making it difficult for flooding to subside.

Another is located in southwestern Taiwan. Unlike the Dongshan River basin, the selected region covers some rivers, including the Erren River, Agongdian River, Dianbao River, Cianjhen River, Houjin Creek, Love River, and Yanshuei River, as well as the main city in southern Taiwan, Kaohsiung. This region is hereafter referred to as the Kaohsiung basin. The area of the Kaohsiung basin is 939.473 km², and the average annual precipitation is about 2000 mm, most of which is concentrated in the summer and autumn. The long-duration flood is typically caused by a tropical cyclone and the southwesterly flow

associated with it. The eastern boundary of the Kaohsiung basin is bordered by the Central Mountain Range, and the rivers generally flow westward toward the Taiwan Strait. This topographic configuration results in short and steep rivers, which respond rapidly to intense rainfall, increasing the risk of flash flooding and overwhelming the urban drainage system during extreme weather events.

2.2 cases overview

Six heavy rainfall events in 2024 and one additional event in 2018 are selected in the study (Table 1). The accumulated precipitation during the flood simulation is shown in Figure 1. The outer circulation of Typhoon Gaemi began affecting Taiwan on the morning of July 23, with the eastern region experiencing the initial impact. The typhoon approached its closest point to Taiwan on July 24 and 25, bringing intense rainfall primarily to northeastern Taiwan. In addition to making direct landfall, Typhoon Gaemi lingered along the coast of Hualien, resulting in prolonged and heavy rainfall across multiple regions before eventually making landfall in Hualien. As the typhoon moved northwest away from Taiwan, it was accompanied by a strong southwesterly flow, which triggered further heavy rainfall in southern Taiwan. Due to the spatial and temporal variation in rainfall intensity, the simulation start times differ for each basin: for the Dongshan Basin, the simulation begins at 04:00 UTC on July 24, 2024, while for the Kaohsiung Basin, it begins at 12:00 UTC on the same day.

Typhoon Krathon affected Taiwan from October 2 to October 4. Due to its slow movement, Typhoon Krathon allowed continuous moisture convergence over the island, enhancing rainfall accumulation in affected regions. On October

3, Typhoon Krathon made landfall in Kaohsiung, causing heavy rainfall and severe flooding in southern Taiwan. In addition to the impact on the south, the typhoon's circulation interacted with prevailing northeasterly winds, resulting in orographic lifting and significant rainfall over northeastern Taiwan, including the Dongshan Basin. To reflect the timing of rainfall onset, different simulation start times were assigned for each basin. For the Dongshan Basin, the simulation begins at 08:00 UTC on October 3, 2024, while for the Kaohsiung Basin, it begins at 00:00 UTC on the same day, aligning with the earlier arrival of heavy rainfall in southern Taiwan.

Typhoon Trami and Typhoon Toraji did not make landfall in Taiwan. Instead, as they passed through the Bashi Channel and the Philippines, they enhanced northeasterly winds, leading to heavy rainfall and resulting localize flooding in the Dongshan Basin. Due to the timing of rainfall, the simulation for the Dongshan Basin begins at 04:00 UTC on the day when heavy rainfall started to intensify under the influence of each respective typhoon, October 24 and November 12, respectively. Since Kaohsiung was not significantly affected by rainfall during these events, no simulations were conducted for the Kaohsiung Basin for these cases.

An additional event that occurred in 2018 was used solely for calibration to enhance the reliability of the model. In 2018, Taiwan was affected by a low pressure in the south, and a tropical low pressure passed through the western coast of Taiwan on August 23~24, and a low pressure system and southwesterly airflow from August 25 to August 28, bringing more than 1,000 millimeters of rainfall to the southwestern region, which resulted in a total of $871.99 million in

agricultural losses and extensive and long-term inundation.

Chapter 3. Data and Methodology

3.1 3Di Hydrodynamic Model

3Di hydrodynamic model (Stelling et al., 2012) is a new simulation software system developed in the Netherlands by Stelling Hydraulics, Deltares, TU Delft, and Nelen & Schuurmans, consisting of a computational core, an application programming interface (API), the modeler interface, and 3Di Live site. The modeler interface provides integration with QGIS so that users can edit or analyze the model visually and interactively. The user can check the simulation in real time by using the 3Di Live site. The simulation results in an inundation data set containing water level, area, and water depth, which users can process additionally. It is good at simulating urban flooding and natural river flow through the simultaneous calculation of surface water movement and its interactions with existing sewer systems. Moreover, 3Di takes advantage of its high resolution and faster simulation speed by applying the quadtree and sub-grid techniques.

3.1.1 Governing equation

The 2D depth-averaged shallow water equations (Stelling, 2012) serve as the foundation, the continuity equation and momentum equations in the x and y directions are as follows:

$$\frac{\partial h}{\partial t} + u\frac{\partial h}{\partial x} + v\frac{\partial h}{\partial y} = 0 \qquad (3.1)$$

$$\frac{\partial u}{\partial t} + u\frac{\partial u}{\partial x} + v\frac{\partial u}{\partial y} + g\frac{\partial \zeta}{\partial x} + \frac{c_f}{h}u\|u\| = 0 \quad (3.2)$$

$$\frac{\partial v}{\partial t} + u\frac{\partial v}{\partial x} + v\frac{\partial v}{\partial y} + g\frac{\partial \zeta}{\partial y} + \frac{c_f}{h}v\|u\| = 0 \quad (3.3)$$

Where $\mathrm{h(x,y,t)}$ is water depth, t is timestep, $\mathrm{u(x,y,t)}$ and $v(x,y,t)$are depth-averaged velocities, g is the acceleration of gravity, c_f represents a dimensionless friction function.

The relationship between water level and water depth is:

$$\mathrm{h(x,y,t)} = \zeta(\mathrm{x,y,t}) - \mathrm{e(x,y)} \quad (3.4)$$

where $\zeta(\mathrm{x,y,t})$ is the water level and $\mathrm{e(x,y)}$ is the bottom elevation.

3.1.2 Computational grid

In 3Di, computational grids are all squares but varying in size, where velocities and discharges are defined at the cell borders, while water levels and volumes are defined at the middle of the cell. The number of computational cells in a simulation has a significant impact on its computational cost. It is always necessary to strike a balance between computing time and grid resolution. To optimize the grid resolution and reduce computational cost, 3Di applies the quadtree method. Figure 2 illustrates the concept of two techniques. The quadtree method splits cells into four quadrants from the coarsest to the finest resolution gradually in areas with small elevation differences. Local grid refinement allows users to concentrate on areas with more intricate flows or where finer-grained findings are needed. Instead, other regions are appropriately simplified to preserve the overall flow characteristics, and the number of computational grids

can be reduced, which helps improve computational efficiency. The maximum quadtree level (kmax) is used to determine the largest possible computational grid size. The relationship is as follows:

$$Largest\ grid\ size = smallest\ grid\ size \times 2^{kmax-1} \quad (3.5)$$

Flow is strongly influenced by the water depth. The flow acts entirely differently, yet the depth is only slightly changed. Therefore, water depth information is essential for accurately simulating flow. Despite the increasing availability of detailed water depth information, it is challenging to incorporate comprehensive grid information without significantly raising computing costs. Subsequently, the sub-grid method is used to find the best balance between accuracy and computing cost. The sub-grid technique is based on grids with different resolutions that allow the water depth to change within a computation grid while the water level remains the same. All input data, such as the DEM, roughness, and infiltration rates, can be specified on the high-resolution grid. However, instead of using a high-resolution grid for simulation, the water levels and velocities can be calculated faster by clustering the high-resolution DEM pixels into calculation grids.

3.1.3 Model configuration

The parameter settings are displayed in Table 2. To develop the flood model, 1m spatial resolution Digital Elevation Model (DEM), along with a roughness map and infiltration map derived from the land use map of the research area, are necessary for the two-dimensional domain; they are illustrated in Figure 3 and Figure 4. Besides infiltration, water can exit the system through boundary

conditions. All boundary conditions in this study are defined in the one-dimensional (1D) domain, with the downstream water level set to -3 meters at the river mouth. This value is chosen to ensure unimpeded discharge into the sea under the assumption of no tidal influence.

In addition, 3Di supports four sewerage structures, including pipes, weirs, orifices, and pump stations. They were built in a one-dimensional network and connected with connection nodes and manholes in the model. In simulations, the model calculates the volume and water level of each manhole, based on the upstream and downstream manhole water levels as well as pipe characteristics.

3.2 Observed rainfall data

Quantitative Precipitation Estimation provides a high-resolution radar observation and quantitative precipitation estimation. The product is adopted as the basis for extrapolation in the MAPLE nowcasting system, calibrating precipitation nowcasting, and running the 3Di model.

3.2.1 Radar network in Taiwan

The composite radar observations are from 4 S-band radars (RCWF, RCCG, RCKT, and RCHL) and 6 C-band radars (RCCK, RCGR, RCLY, RCMK, RCNT, and RCSL), the locations of 10 radars are displayed in Figure 5.

The Composite Reflectivity data provides the most complete observation of reflectivity data, with 0.0125° horizontal resolution and 10-minute temporal resolution. Coverage from 115°E to 126.5°E, 18°N to 29°N, serves as the input for applying VET. For assessing forecast performance of MAPLE and used as the

input of 3Di, the reflectivity is converted to rain rate by the Z-R relationship (Chen et al. 2017).

$$\mathrm{Z} = 223.04 \times R^{1.51} \quad (3.\ 6)$$

3.2.2 QPESUMS

Quantitative Precipitation Estimation and Segregation Using Multiple Sensors (QPESUMS) was obtained from the Central Weather Administration (CWA), is an operational product derived from different precipitation estimate algorithms based on the characteristics of each radar, and is further corrected with rain gauge observations (Chang et al., 2021). This product provides 1-h accumulated precipitation in a 10-minute time interval.

Another QPE product is QPESUMS10M, which is experimental and provides 10-minute accumulated precipitation every 10 minutes. However, QPESUMS10M is not corrected with rain gauge observations and is only available after September 2022. These two products have the same spatial (0.0125°) and cover the same spatial window from 118°E to 123.5°E, and 20°N to 27°N.

Even though the two QPEs are not exactly equal (one is calibrated by the rain gauges), we use both of them instead of two experimental products, such as QPESUMS10M, and QPESUMS10M accumulate to one hour, is due to QPESUMS is the most accurate operational QPE available.

3.3 MAPLE nowcasting system

McGill Algorithm for Precipitation nowcasting by Lagrangian Extrapolation (MAPLE) is a nowcasting system developed by the J. S. Marshall Radar Observatory of McGill University. MAPLE determines the motion field based on the prior radar echo data using Variational Echo Tracking (VET). Then it generates a nowcast by a semi-Lagrangian backward scheme during the forecast period.

3.3.1 Variational Echo Tracking (VET) technique

The VET technique, originally described by Laroche and Zawadzki (1995), derives the velocity field of radar reflectivity echoes. Here, we apply this to calculate the motion field of the composite radar network. The cost function can be represented through the following two constraints:

$$J_{VET}(\boldsymbol{u}) = J_{\Psi} + J_V \tag{3. 7}$$

u is the two-dimensional motion vector, calculated by minimizing the cost function. The function J_{Ψ} is defined as the conservation of reflectivity constraint which is the sum of squares of the echo residuals in the domain, J_V is a smoothness penalty function that smooths the motion field by the second-order space derivative. They may be respectively expressed as follows:

$$J_{\Psi} = \iint_{\Omega} \beta(\mathrm{x}) \left[\Psi(t_0, \mathrm{x}) - \Psi(t_0 - \Delta\mathrm{t}, \mathrm{x} - \mathbf{u}\Delta\mathrm{t})\right]^2 dx\, dy \tag{3. 8}$$

where β(x) is the weight assigned to this smoothness constraint, Ψ is the

observation of reflectivity, x is position, t_0 is the initial forecast time, and Δt is the time interval between two consecutive observation echoes.

$$J_v = \gamma \iint_{\Omega} \left[\left(\frac{\partial^2 u}{\partial x^2} \right)^2 + \left(\frac{\partial^2 u}{\partial y^2} \right)^2 + 2 \left(\frac{\partial^2 u}{\partial x \partial y} \right)^2 + \left(\frac{\partial^2 v}{\partial x^2} \right)^2 + \left(\frac{\partial^2 v}{\partial y^2} \right)^2 + \left(\frac{\partial^2 v}{\partial x \partial y} \right)^2 \right] dx\, dy \quad (3.9)$$

where γ is the weight of the smoothness constraint, u and v are the motion vectors of reflectivity in axis-x and axis-y, Ω is the domain of the motion field calculation. The optimal motion field is found by gradually increasing the resolution using the scaling-guess approach created by Laroche and Zawadzki (1994) to prevent the likelihood of convergence towards a secondary minimum. It is to be noted that the motion vector is more reliable in precipitation area rather than isolated echoes or no-echo region. There are some adjustable parameters which are number of images, time interval of images, reflectivity threshold, relative weights β and γ , number of scaling guesses, vector density of each scaling guess, amount of smoothing, and temporal smoothing. The parameters setting is displayed in Table 3.

3.3.2 Semi-Lagrangian advection

Once the VET technique has been utilized, the motion field is interpolated at each grid point using bilinear interpolation. Germann and Zawadzki (2002) developed a semi-Lagrangian approach that can be used to generate the nowcasts:

$$\tau = N\Delta t \quad (3.10)$$

$$\alpha = \Delta t \mathbf{u}\left(t_0, x - \frac{\alpha}{2}\right) \quad (3.\ 11)$$

where τ is the length of forecast time, and α is the displacement vector. The advection scheme can be divided into N timesteps (Δt). Thus, we can generate the suitable α from $\mathbf{u}$ with respect to each timestep. In this method, the displacement of the system, including rotation, can be well simulated.

3.4 Experiment setting

The two figures (Figure 6) illustrate the distribution of rainfall intensity (mm per 10 minutes) during major rainfall events in Northeastern and Southwestern Taiwan, which cover the study area (Figure 7). Both regions exhibit a decay distribution, where lower rainfall intensities are far more frequent than extreme ones. However, the characteristics of rainfall events differ between the two regions in terms of frequency and intensity. For northeastern Taiwan, the most frequent rainfall intensity is 0.5 to 1 mm/10min with 464,068 occurrences, and gradually decreases as intensity increases. The maximum recorded rainfall is 36.5 mm/10min, and 291 occurrences exceeded 20 mm/10min, demonstrating that such extreme events are possible and measurable. For southeastern Taiwan, the most frequent rainfall bin is slightly higher, around 2 mm/10min (541,035 occurrences), indicating a tendency for heavier moderate rainfall compared to the Northeast. The maximum recorded rainfall is 81.1 mm/10min, showing that extremely high rainfall rates can develop. Also, 3,042 occurrences exceeded 20 mm/10min, confirming that these events are not isolated and must be considered in hydrological analysis. Given this, setting 20 mm/10 min as an idealized rainfall

intensity for 3Di simulations is essential to assess potential impacts.

The rainfall exceeding 20 mm in 10 minutes is possible to occur due to tropical cyclones or other weather systems, and knowing when and where is critical. To accurately capture these events, a 10-minute Quantitative Precipitation Estimation (QPE) system providing 10-minute accumulated rainfall is necessary. However, the operational QPE product in Taiwan, QPESUMS, only provides a 10-minute time resolution but one hour of accumulated precipitation. This will provide real-time monitoring, helping to identify areas experiencing intense rainfall.

For QPESUMS and QPESUMS10M, precipitation is fed directly into 3Di with their respective temporal resolutions, hourly and 10 minutes. For QPN from MAPLE, we generate a 1-hour-long time series of nowcast precipitation every hour with a temporal resolution of 10 minutes. Using the Z-R relationship, hourly precipitation can be derived from reflectivity. The following three nowcast strategies have been applied: Radar echo data is transformed into precipitation over 10-minute, 30-minute, and 60-minute intervals using the Z-R relationship. These QPN are then fed into the 3Di model every 10 minutes, 30 minutes, and 60 minutes, referred to as MAPLE10mins, MAPLE30mins, and MAPLE60mins, respectively. The diagram is shown in Figure 8.

Figure 9 illustrates the overall workflow of the inundation simulations conducted in this study. Three different rainfall inputs were used to drive the hydrodynamic model: (1) the original QPESUMS radar rainfall product, (2) an experimental version of QPESUMS with 10-minute accumulated rainfall (referred to as QPESUMS10M), and (3) MAPLE nowcast rainfall data. Each

precipitation input was independently applied to the 3Di hydrodynamic model to generate corresponding flood simulations: QPESUMS-based, QPESUMS10M-based, and MAPLE-based inundation results. This framework allows for a comparative assessment of the sensitivity of flood modeling outcomes to various types of rainfall input, encompassing both observed and forecasted data. The comparison between QPESUMS and QPESUMS10M enables the evaluation of the benefits of higher temporal resolution, while the MAPLE nowcast performance is assessed using the QPESUMS simulation as a benchmark.

Chapter 4. Verification strategies

4.1 Observed flood data

In the past, real-time flood data relied solely on reports from affected residents and EMIC notification, who typically describe flooding as reaching knee height, half a wheel high, or an approximate depth. After a flood, government personnel conduct on-site investigations but often rely on resident interviews and water marks left behind to estimate flood depth. Fortunately, a more comprehensive set of observational data is available in selected cases, including EMIC, flood sensors and satellite data, which improve the validation of the 3Di flood model. EMIC data offers single-time measurements of general water depth in a specific area. Though it lacks temporal continuity, it contributes to understanding flood conditions at key moments. Meanwhile, the flood sensors provide continuous time series data at specific locations, capturing detailed water

depth variations over time. This allows for high temporal resolution validation of model simulations. Additionally, satellite data offer a general flood extent at specific time points, providing a spatial overview of inundated areas. This data is crucial for large-scale validation, complementing the localized but high-frequency measurements from flood sensors.

By integrating all three data sources: EMIC data, flood sensors, and satellite imagery, we can maximize the validation of the 3Di model, ensuring that both temporal and spatial aspects of flooding are accurately represented. This multi-source approach strengthens confidence in the model's ability to simulate real-world flood events, making it a more reliable tool for flood forecasting and risk assessment. Table 4 displays the data availability in different cases. Red represents unavailable or lacking data, while green indicates available data. There is only a limited EMIC record in Dongshan, while there are more consistent records in Kaohsiung. The flood sensors in Taiwan were installed after 2022, meaning that historical flood events before this period lack sensor data. Moreover, Sentinel-1 successfully captured post-flood images within hours of key events on 2018-08-23, 2024-07-24, and 2024-11-12, demonstrating its effectiveness in flood monitoring. However, there are noticeable data gaps in both EMIC and SAR records, particularly in events such as 2024-10-03 and 2024-10-24, which could affect flood assessment in those cases. Overall, Dongshan has fewer data points compared to Kaohsiung.

4.1.1 EMIC

Emergency Management Information Cloud (EMIC) is a cloud-based

information integration platform. Developed in collaboration with the Taiwanese Fire Department, it enhances emergency preparedness and response efficiency by collecting, analyzing, and sharing diverse emergency data. The system includes data on various types of disasters, such as floods, earthquakes, and fires. Specifically, the system includes flood information on water depth, notification time, locations, descriptions of the severity, and the impacted areas, which are frequently used to validate flood models in the early stages. However, incomplete or incorrect information will affect the reliability of the data.

4.1.2 Flood sensor

The point-based flood sensors, where installed roadside, measure water depth and send the data back to the cloud monitoring system. These sensors provide data for real-time flood disaster warnings, flood model validation, and flood extent estimation. Chang et al. (2024) evaluated the accuracy and reliability of these sensors in detecting flood events and confirmed their value in enhancing flood modeling and decision support. Their findings support using sensor data as a reliable reference for real-time applications and post-event model validation in this study. Currently, over 2300 flood sensors have been installed across Taiwan; the location is mainly based on elevation, historical events, and flood hotspots. There are, respectively, 37 and 146 flood sensors in Dongshan and Kaohsiung; their location is displayed in Figure 10.

4.1.3 SAR

Synthetic Aperture Radar (SAR) signals are mirrored on smooth, open water

surfaces, resulting in lower backscatter values. Since SAR can penetrate cloud cover and remain unaffected by adverse weather conditions, it is widely used for flood detection. However, for SAR to be effectively used, the imaging time must correspond accurately to the flood event. Significant terrain variations can cause radar shadowing and strong reflections in urban areas, making it difficult to detect water bodies properly. Moreover, SAR performs best in detecting areas that are completely covered by water, while partially flooded regions may be harder to identify.

SAR data used for flood monitoring comes from Sentinel-1, a C-band radar satellite operated under the Copernicus Programme by the European Space Agency (ESA). The Level-1 Ground Range Detected (GRD) product with VV polarization undergoes pre-processing, which includes applying orbit files, radiometric calibration, multilooking, speckle reduction, and terrain correction.

Flood detection is addressed as a binary segmentation problem using bi-level thresholding and a simple histogram analysis, where the goal is to distinguish dark pixels from brighter ones. Darker pixels typically indicate flooded areas, while brighter pixels correspond to non-flooded regions. In this study, the threshold values of -10 dB for Kaohsiung and -15 dB for Dongshan are applied based on the histogram analysis, as shown in Figure 11. The 5 dB difference between the two thresholds may be attributed to differences in radar incidence angles and surface water characteristics, which influence the backscatter intensity observed in the images.

4.2 Verification approaches

4.2.1 Continuous Verification

The spatial correlation coefficient (SCC) from continuous verification and the root mean square error (RMSE) are used to assess the nowcasting system's performance. The degree of similarity between the forecast and the observation can be evaluated by the SCC. The SCC can be written as follows:

$$SCC = \frac{\sum(F - \bar{F})(O - \bar{O})}{\sqrt{\sum(F - \bar{F})^2 (O - \bar{O})^2}} \quad (4.\ 1)$$

where F and O denote the total rainfall of the prediction and the observation, and $\bar{F}$and $\bar{O}$ are an area average over a two-dimensional precipitation field. SCC varies between 0 and 1, the latter being the ideal value. The RMSE measures quantitatively the deviation between the forecast and the observation. The definition of the RMSE is as follows:

$$RMSE = \sqrt{\frac{\sum_{i=1}^{N}(F - O)^2}{N}} \quad (4.\ 2)$$

Where N is the total number of grid points. RMSE varies between 0 (perfect match) and $+\infty$.

4.2.2 Categorical verification

Categorical verification is to assess the capability of different levels of flood, precipitation, or another signal by a binary threshold. It is used to compare the

3Di model and other observational flood data. Each grids in the model domain are classified into one of four categories in a confusion matrix (Table 5), which is based on whether the flood was correctly predicted. The hit (a) represents the number of cases where both the simulation and observation identify a flood. The miss (b) occurs when a flood is observed but not simulated. The false alarm (c) refers to a flood identified by the simulation but not observed. The correct negative (d) indicates cases where both the simulation and observation agree that no flood occurred. In this study, the probability of detection (POD), the false-alarm rate (FAR), the accuracy, the bias, and the critical success index (CSI) of the categorical verification are formulated as:

$$POD = \frac{a}{a+b} \tag{4. 3}$$

$$FAR = \frac{c}{a+c} \tag{4. 4}$$

$$Bias = \frac{a+c}{a+b} \tag{4. 5}$$

$$CSI = \frac{a}{a+b+c} \tag{4. 6}$$

$$Accuracy = \frac{a+d}{a+b+c+d} \tag{4. 7}$$

where the range of POD, Accuracy, and CSI are from 0 to 1, with a perfect score of 1. FAR also has a range of 0 to 1, while the best value is 0. The ratio of the forecasted event to the observed is known as bias, ranges from 0 to ∞, and is perfect in 1. The forecast overstated the events if the bias was bigger than 1.

4.2.3 Neighborhood method

While binary verification methods provide a general summary of model performance, more insights can be gained through a scale-selective approach, which is based on the Fraction Skill Score (FSS), providing additional insights by considering spatial scale variations in forecast skill. This technique, widely used in atmospheric sciences for evaluating precipitation forecasts (Roberts and Lean, 2008), applies a neighborhood-based method to assess how well forecasted patterns align with observations across different spatial scales. Hooker et al. (2022) demonstrated that FSS can be effectively applied to flood inundation verification using SAR data, as it works well with 2-D flood maps where each grid cell is classified as either flooded or unflooded.

A neighborhood approach based on the Fraction Skill Score (FSS) that considers uncertainty in spatial scale. Firstly, we interpolated the SAR data from 10m to 1m, the same as the 3Di flood map. Then, assign each grid cell as flooded (1) or unflooded (0) by the same threshold that has been defined previously in both SAR and 3Di. The FSS is defined as:

$$FSS_n = 1 - \frac{\frac{1}{N_x N_y}\sum_{i=1}^{N_x}\sum_{j=1}^{N_y}\left[O_{nij} - F_{nij}\right]^2}{\frac{1}{N_x N_y}\sum_{i=1}^{N_x}\sum_{j=1}^{N_y}\left[O_{nij}^2 + F_{nij}^2\right]} \quad (4.\ 8)$$

where N_x and N_y represents the number of interested domain, O is the observation, F is the model data. The neighborhood is determined in n, a square form as $n \times n$ surrounding the grid cell. For instance, if n=1, only a single grid is calculated. On the other hand, when n=3, then 9 grids are taken into account.

FSS of 1 is said to have perfect skill, and 0 means no skill. The spatial scales n=11,15,19,23,27,31 were selected by considering the different original resolutions of the model and SAR data.

Chapter 5. Results and discussion

An idealized experiment with three different total rainfall scenarios is first displayed in section 5.1. Secondly, the forecast skill of MAPLE is examined in section 5.2. The validation of the 3Di model with multiple flood observational data is shown in section 5.3. In section 5.4, the discrepancy between QPESUMS and QPESUMS10M is evaluated. The results of all real cases with QPESUMS, QPESUMS10M, and MAPLE are shown in sections 5.4 and 5.5.

5.1 Idealized experiment

Figure 12 illustrates the 5-hour designed rainfall simulation, inundation area for 20 mm distributed evenly in 10 minutes, 30 minutes, and 60 minutes in Dongshan. Three idealized scenarios achieve a flood peak at the moment when the rain ends, following which the inundation area gradually descends in the next few hours. The scenario of 20 mm concentrate within 10 minutes has a sharp increment in flood area, it is the earliest to hit the peak, and also has more inundation area than others. On the other hand, the other two scenarios show a slight difference in the peak value, but differ in the time to reach peak.

The bar charts (Figure 13) compare the percentage of flooded and unflooded areas under two different rainfall distributions: concentrated within 10 minutes and equally distributed over 60 minutes, the x-axis shows the variation of total

rainfall. Each grid cell is classified into one of four conditions: flooded in both rainfall scenarios, flooded only under the 10-minute concentrated rainfall, flooded only under the 60-minute evenly distributed rainfall, or unflooded in both scenarios. In both locations, as total precipitation increases, the flooded area expands while the unflooded area decreases. The pink bars represent areas flooded under the 10-minute concentrated rainfall but remained unflooded under the 60-minute evenly distributed rainfall, showing a growth when the total precipitation increases. In contrast, the charts with values of zero indicate that no areas were flooded under the 60-minute distribution while remaining unflooded under the 10-minute scenario. It is evident that when rainfall is concentrated in a short period, some areas experience flooding, whereas the same total precipitation distributed over a longer duration does not cause flooding.

Eventually, the root mean square difference (RMSD) among the flood pixels is displayed in Figure 14, comparing the difference between 20 mm distributed evenly in 10 minutes, 30 minutes, and 60 minutes in both locations. In both plots, the RMSD values generally decrease as total rainfall increases from 10 mm to 40 mm. This is because the RMSD calculation only considers grid points where flooding occurs (water depth > 0.1m). When the total rainfall is low, fewer grid points meet this criterion, which can amplify differences. As rainfall increases, more grid points experience flooding, leading to a more stable and representative comparison, which reduces the observed RMSD differences. This can also explain the difference between the two places, the RMSD is computed over a smaller subset of the domain, making localized variations more significant. The blue line (60 mins vs. 10 mins) consistently shows higher RMSD values than the orange line (30 mins vs. 10 mins). This suggests that the water depth differences

are more pronounced when comparing 60-minute rainfall with 10-minute rainfall than when comparing 30-minute with 10-minute rainfall. In other words, shorter, more intense rainfall (10 mins) leads to more significant differences in water depth compared to longer durations (60 mins).

The result emphasizes the importance of rainfall intensity in flooding, showing that short, intense rain is more likely to overwhelm drainage systems and lead to flooding. The result indicates that if we only use one-hour-resolution precipitation data to drive the hydrological forecast, we may underestimate and delay the forecast because we cannot tell the difference if we only have coarse-time resolution data.

5.2 Validation of 3Di with observational flood data

5.2.1 Using EMIC and flood sensors as a reference

EMIC data records inundation points during flood events, providing a valuable reference for model verification. Given the relatively abundant data available for Kaohsiung, we focus on utilizing EMIC data primarily for this region. Table 6 presents the number of EMIC records in each case of Dongshan and Kaohsiung. Figure 15 illustrates the extent of flooding simulated by the 3Di model and the distribution of EMIC points. In these three events, a significant concentration of EMIC points is observed in the southern part of the domain, characterized by lower elevation and dense urbanization, which appears to be at higher risk of flooding. According to the number and the distribution of EMIC, the case of 2024-07-24 is the most widespread flooding, particularly in the central

region. The flooding of 2018-08-23 is also evident, particularly in the northern region. Compared to the previous two events, 2024-10-03 has the least flood area and EMIC points, and is concentrated only in the south. Table 7 presents the detection rate of the model simulation compared with EMIC. The event of 2024-07-24 has the highest agreement (95%), suggesting that most inundation points can be captured correctly by the 3Di model. The other two cases have about 80% detection rate, indicating a marginally lower performance.

Based on the model's predictions and the actual observation, accuracy quantifies the proper identification and classification of flooded or unflooded areas. Figure 16 presents the accuracy across different cases. The results indicate a notable discrepancy in performance between the two locations, with Kaohsiung outperforming Dongshan. The Kaohsiung cases demonstrate superior classification performance, with all instances surpassing the 0.5 accuracy threshold. In contrast, the accuracy of Dongshan exhibits greater variability, with some cases achieving moderate performance, while the case of 2024-07-24 in Dongshan records the lowest accuracy, failing to reach 0.5, suggesting limitations in the model's predictive capability for that event. This is because there are only 37 flood sensors in Dongshan, significantly fewer than the 146 sensors in Kaohsiung, making the performance more sensitive. However, when working with unbalanced datasets, when one class hugely outnumbers the others, its reliability declines. Since there are usually far fewer flooded samples than non-flooded ones, this problem is especially important to flood categorization; relying only on the metric may result in an overoptimistic estimation of the classifier's performance.

To tackle this limitation, performance diagrams were obtained in the study. Several forecast accuracy verification metrics are shown in the performance diagram (Roebber et al. 2009). The upper-right corner of the diagram represents the best forecast quality, when POD, the successive ratio (1-FAR), BIAS, and CSI all approach 1. The region of warm color indicates that CSI > 0.6. The dashed line indicates BIAS, and the forecast is unbiased if the diagonal equals 1. Figure 17 shows the diagram of 4 cases in Dongshan and 2 cases in Kaohsiung, using flood sensors as reference. Three of the cases in Dongshan had similar success ratios around 0.4 and a CSI around 0.5, but only 1 had the POD close to 1. They tended to underestimate due to the small BIAS and POD. On the other hand, in the other cases, they performed POD above 0.7; however, there was a wide range in success ratios, about 0.3 to 0.7, indicating an overestimate due to the BIAS above 1.

5.2.2 Using SAR data as a reference

By the same token, the verification technique was further applied to SAR data. Figure 18 illustrates the distribution of EMIC points and the SAR detection in Kaohsiung. It is found that SAR only detects a small flood area in the densely recorded areas due to the urban area has a high backscatter value, whether there is water or not. Secondly, the northeast region has plenty of signals, which are considered to be the radar shadow caused by the terrain. Hence, we only focus on the domain in the red frame rather than the whole domain. For Dongshan, we remain to obtain the whole region. Figure 19 shows the accuracy across different events, using SAR data as a reference. These cases were selected because of their

availability of SAR data, including 2024-07-24 in both locations, 2024-11-12 in Dongshan, and the additional case 2018-08-23 in Kaohsiung. Apparently, all cases with accuracy far surpass the threshold, outperforming the one using flood sensors. Specifically, the event occurred in the Dongshan exhibit a greater performance; it is possibly caused by the geographical feature, a wide range of wetland in the northeastern in the basin. Water-covered areas, such as wetlands or lakes, are easier to detect by SAR because its signals are reflected on a smooth water surface. As a result, hits would rise in proportion to the area the SAR detected. For Kaohsiung, the accuracy of 2018-08-23 is slightly greater than 2024-07-24; a possible reason is that there may be a more severe flood on 2018-08-23 in the north region, which was our focus area, according to the spatial distribution of the EMIC report.

Figure 20 illustrates the performance diagram taking the SAR data as reference. The case of 2018-08-23 stayed close to the top right corner of the diagram, having the best performance. Except for this, all cases demonstrate a great success ratio of about 0.8 to 1, meaning that the low false alarm rate. However, the cases of 2024-07-24 in both locations and 2024-11-12 in Dongshan have a small POD, from 0.2 to 0.4, showing an underestimation by the model.

The model's performance is statistically assessed using the neighborhood approach. Figure 21 illustrates the Fractions Skill Score (FSS) across varying neighborhood sizes (from 11 to 31) for different events and model configurations. Given that the original SAR dataset has a spatial resolution of 10 meters, the smallest neighborhood considered is 11 m × 11 m to align more meaningfully with the input data's native resolution. All curves show a gradual upward trend,

indicating marginal improvement in FSS as the neighborhood size increases. This improvement results from larger neighborhoods smoothing out discrepancies between predicted and observed values, thus improving FSS. Notably, the events in Dongshan consistently exhibit higher FSS values across all neighborhood sizes, likely due to the higher proportion of wet areas in the basin, which enhances spatial agreement. In contrast, events in Kaohsiung demonstrate lower FSS scores, suggesting less spatial consistency between predictions and observations.

Overall, while the neighborhood method yields some improvement in FSS, the gains are modest, highlighting the already strong spatial performance of the model at the native resolution. If two-dimensional observational data with a resolution closer to the model's native grid were available, it would further enhance the reliability and precision of the validation process. Nevertheless, there are still significant drawbacks to SAR-based flood monitoring, particularly in urban and vegetated places where complex scattering mechanisms may make it difficult to accurately identify water regions.

5.3 Comparison between QPESUMS and QPESUMS10M

Figure 22 presents the spatial distribution of average differences between QPESUMS10M accumulated to one hour and QPESUMS for different events, with red areas indicating higher values in QPESUMS10M and blue areas showing higher values in QPESUMS. The maps reveal distinct spatial patterns in precipitation discrepancies, highlighting regional variations in overestimation and underestimation. In Dongshan, the QPESUMS10M dataset tends to underestimate rainfall compared to QPESUMS. However, localized

overestimations appear in certain events, suggesting variations in short-duration rainfall capture. In contrast, Kaohsiung exhibits a more consistent overestimation pattern, where QPESUMS10M shows higher rainfall amounts across larger areas, particularly in heavy rainfall cases. The event on 2024-07-24, influenced by Typhoon Gaemi, shows widespread discrepancies with large regions of overestimation and underestimation, reinforcing the high dispersion seen in the scatter plots. These spatial differences indicate that QPESUMS10M may struggle to accurately capture localized convective storms or extreme rainfall, which has implications for hydrological modeling and flood forecasting.

Figure 23 presents the precipitation results for each hour in the events, showing density scatter plots comparing the QPESUMS10M sum up to one hour (x-axis) with the QPESUMS (y-axis). Figure 23 a-d present the area in Dongshan, Figure 23 e-f present the area in Kaohsiung. The overall distribution of the scatter plot in each location between events is quite different, but all display a high density on the line of y = x in smaller rainfall amounts, along with a high correlation coefficient. In Dongshan, the density of three events (2024-07-24, 2024-10-24, and 2024-11-12) is higher above the y = x line, indicating that QPESUMS10M tends to have weaker precipitation than QPESUMS. Conversely, in the other events, the QPESUMS10M has more intense precipitation than the QPESUMS, especially in Kaohsiung. This suggests that in Dongshan, short-duration rainfall is often underestimated by QPESUMS10M, while in Kaohsiung, QPESUMS10M overestimates precipitation, possibly due to convective storm activity. Additionally, on 2024-07-24, Typhoon Gaemi led to significant rainfall in both regions, causing a greater dispersion of grid points and a regression line that deviates more from y = x compared to other events. The high variability

observed indicates that high-intensity convective bursts that are not evenly distributed within an hour may introduce biases in hydrological and flood modeling.

Although the overall differences between QPESUMS and QPESUMS10M may not appear extreme, their impact on flood modeling is significant. Figure 24 and Figure 25 reveal that when QPESUMS10M and QPESUMS are used as input for the 3Di flood model, the simulated inundation area of QPESUMS10M is consistently larger, and the flood peaks occur earlier across all events and both locations. This suggests that the finer temporal resolution allows for the earlier detection of flooding, which is particularly important for early warning systems and disaster preparedness. Furthermore, the relationship between rainfall intensity and flood area growth indicates that QPESUMS10M's higher resolution enables a more responsive simulation of hydrological processes. When rainfall intensity is higher, the difference between the flood areas produced by the two datasets is more pronounced. This suggests that high-resolution precipitation data can better capture short-duration, high-intensity rainfall events, leading to more realistic flood forecasts. Given these findings, further analysis is necessary to quantify the impact of different precipitation inputs on hydrological simulations.

5.4 Evaluation of MAPLE's forecast performance

The forecast skill of MAPLE can be evaluated by comparing the predicted precipitation field with QPESUMS. The Z-R relationship in (3. 6) converts the predicted precipitation field from reflectivity(Z). To better assess the performance of the data used, we validated the rainfall field based on the strategy applied in

the 3Di model, specifically focusing on the rainfall over land. The heat map in Figure 26 presents SCC values of one-hour accumulated precipitation between the three nowcast strategies and QPESUMS across four events. SCC values above 0.5 indicate predictive ability. In all cases, MAPLE10mins consistently exhibits more blue regions and remains relatively stable throughout the day. In contrast, MAPLE30mins is sometimes close to MAPLE10mins but fluctuates more. However, MAPLE60mins displays more red regions, indicating the lower SCC and the weakest performance.

RMSE was calculated to quantitatively assess the errors of the 3 strategies of nowcast. As shown in Figure 27, MAPLE10mins consistently has the lowest RMSE, while MAPLE30mins follows closely behind. MAPLE60mins has the highest RMSE in all cases, showing that longer durations lead to increased errors. In the cases of 2024-07-24 and 2024-10-03, they both showed significant fluctuation, with peaks reaching 15 mm and 10 mm at certain hours, respectively. These are likely due to increased rainfall caused by the landfall of the tropical cyclones in these cases. On the contrary, in 2024-10-24 and 2024-11-12, RMSE are relatively lower, with less variability over time. Overall, although the value of SCC and RMSE is case-dependent, the result shows that MAPLE10mins is the most reliable forecast across all cases.

5.5 Hydrological value of MAPLE forecasts

Figure 28 illustrates the inundation area across events, comparing the performance of various precipitation inputs: QPESUMS, QPESUMS10M, and MAPLE at different input intervals (10, 30, and 60 minutes). Figure 28 a-d are in

Dongshan, Figure 28 e and f are in Kaohsiung. Figure 28 a illustrates the temporal evolution of the flood inundation area, beginning from 04:00 UTC on July 24, 2024. A clear divergence in flood extent is observed, particularly during the peak period between 09:00 and 12:00, where QPESUMS10M shows the highest inundation area, peaking above 20 km², QPESUMS displays a slightly lower peak (around 17 km²), while the MAPLE-based forecasts show relatively consistent results with a peak near 15 km², regardless of the temporal resolution. The MAPLE outputs remain more stable across the event, reflecting potentially more smoothed rainfall estimates. MAPLE forecasts show lower flood extents overall, indicating a tendency to underestimate inundation compared to QPESUMS and QPESUMS10M. In Figure 29, the reflectivity fields are similar, a strong rainband of a tropical cyclone is moving in, however, there are significant differences in the rainfall field comparing the result of Z-R conversion and QPESUMS10M. In addition, MAPLE with a 60-minute update interval appears less smooth than 10mins and 30mins, showing more fluctuation across the timeline. While the timing of the peak rainfall is similar across all methods, the recession (drainage) rate differs, with MAPLE showing a distinct pattern from QPESUMS, possibly due to differences in rainfall accumulation.

Figure 28b illustrates the flood inundation area starting from 08:00 UTC on October 3, and shows a comparatively smaller event than in Figure 28a. The results indicate that QPESUMS10M and QPESUMS forecast larger inundation areas, peaking around 15:00–16:00, with maximum extents of approximately 10 km² and 8 km², respectively. In contrast, all MAPLE forecasts (10, 30, and 60mins) remained under 2 km² throughout the simulation period. This underestimation is primarily attributed to forecast error. A detailed comparison of the reflectivity

fields reveals a key discrepancy (Figure 30 and Figure 31): in the observed data, a convective system develops directly over the Dongshan basin, while in the forecast fields, this system is entirely absent. This highlights a fundamental limitation of nowcasting systems, difficulty in detecting and forecasting new, rapidly developing convective cells, particularly when they initiate locally and are not connected to pre-existing echoes.

Figure 28c displays the flood inundation area starting from 04:00 UTC on October 24. The QPESUMS data reveals two distinct peaks in inundation extent. MAPLE products, particularly MAPLE10mins, accurately capture the timing and magnitude of the first peak, demonstrating their capability in reflecting the initial rainfall event. However, significant discrepancies emerge during the second peak. All MAPLE variants, especially MAPLE60mins, exhibit substantial overestimations of the inundated area compared to QPESUMS. To further investigate this divergence, a comparison between forecast fields and observed rainfall was conducted (Figure 32). Observational data indicate the presence of a strong rainband, which slightly weakened in the subsequent hour. In contrast, MAPLE showed the strong rainband moving directly into the basin, which did not occur in the observation. This caused a sharp increase in the simulated flood area and led to an overestimation of the flooding extent. Among the MAPLE products, since MAPLE60mins assumes a constant rainfall rate over one hour based on a single nowcast, it tends to smooth over temporal variability and exaggerate the impact of forecasted intense rainbands. In contrast, MAPLE10mins, despite relying on the same hourly nowcast, introduces rainfall into the hydrological model at a finer temporal resolution, which results in simulations closer to those based on QPESUMS10M. This emphasizes that not

only the forecast accuracy but also the temporal resolution of rainfall input plays a crucial role in flood simulation outcomes.

Figure 28d presents the simulated flood area starting at 04:00 UTC on November 12, 2024. In this case, both QPESUMS and QPESUMS10M show a rapid rise in inundation extent during the early hours, peaking around 08:00–09:00 UTC. The MAPLE-based simulations generally follow the same trend, with MAPLE10mins closely capturing the timing and magnitude of the peak flood area, though with some underestimation during the initial rapid increase. Interestingly, all MAPLE simulations show a smoother flood area evolution compared to QPESUMS, especially during the rising limb, suggesting limitations of position errors of the rainband or Z-R conversion. Figure 33 displays the difference between the forecast and the observation. Despite using the same forecast inputs, the difference in rainfall input frequency plays a key role. MAPLE60mins tends to produce the smoothest and most delayed flood response, while MAPLE10mins shows better agreement with QPESUMS10M, reflecting the benefit of higher temporal resolution when simulating rapid flood events. However, all MAPLE simulations exhibit a similar rate of decrease during the recession limb, closely matching the trend observed in the two QPE-based simulations, indicating that the recession phase was well captured in the forecasts.

The inundation areas for the Kaohsiung cases on 2024-07-24 and 2024-10-03 are shown in Figure 28 e and f, respectively. The shape of the flood area curves across all datasets is generally consistent, indicating that the nowcasting approach is able to capture the overall flood trend reasonably well. However, MAPLE consistently underestimates the inundation extent compared to QPESUMS10M

and QPESUMS, particularly in the more intense event on 2024-07-24. This suggests that while the nowcasts reflect the temporal pattern of rainfall, their intensity, especially during high-rainfall events, may be insufficient to accurately reproduce peak flood conditions.

Overall, the results demonstrate that MAPLE nowcasts, despite certain limitations in capturing localized convective developments, still offer meaningful value in hydrological simulations. Particularly, the consistency in trend reproduction and the reasonable performance in capturing peak timing, especially under the 10-minute input scheme, suggest that MAPLE can effectively support flood forecasting when high-frequency input is applied. While it tends to underestimate flood extent in intense events, its smoother rainfall estimates reduce noise and yield stable flood area simulations, which may be advantageous in operational forecasting. These findings indicate that MAPLE can contribute valuable input to flood models. In addition, the results indicate that smaller basins like Dongshan are more sensitive to the accuracy of precipitation inputs, where errors in nowcast rainfall fields more directly translate into discrepancies in flood extent simulations.

Chapter 6. Conclusion and future work

6.1 Conclusion

In this study, we investigate the ability of high temporal resolution precipitation data to improve flood simulation accuracy in 6 cases. Two QPE products and the forecast by MAPLE are assessed and fed into the 3Di model.

Furthermore, the flood model was validated by the observational flood data with improved data availability from these events. The forecast results of MAPLE are evaluated by continuous verification with SCC and RMSE, categorical verification with accuracy, performance diagram, and neighborhood method. The following is a summary of the study's findings:

1. To understand the impact of rainfall intensity distribution on flooding, this study examines different rainfall durations with equal total precipitation. The results show that short-duration, high-intensity rainfall leads to faster and more extensive flooding compared to longer-duration events. This difference in flood response highlights how rainfall intensity, not just total amount, influences flood risk. The findings suggest that using coarse temporal resolution in hydrological modeling may underestimate flood potential and delay warnings, underscoring the need for high-resolution precipitation input for accurate forecasting and flood simulation.

2. To validate the 3Di flood model, this study uses EMIC observational flood points as reference, focusing on Kaohsiung due to its richer data. The results show a strong agreement between simulated and observed inundation for the 2024-07-24 event, with a 95% detection rate. Other cases also reach about 80%, confirming reasonable model performance. However, classification accuracy varies by region, with Kaohsiung consistently outperforming Dongshan. In Dongshan, low accuracy in some cases highlights limitations in predicting complex flood patterns. Due to the imbalance in flood and non-flood samples, performance diagrams were applied for more reliable

verification. The diagrams reveal a mix of underestimation and overestimation depending on the event, emphasizing the need for careful evaluation when applying flood simulation in diverse terrains.

3. SAR data provides another validation source, offering full spatial coverage. When compared with 3Di outputs, SAR-based accuracy is generally higher than that of flood sensor comparisons, especially in Dongshan, where wetlands enhance water detection. However, SAR data is less reliable in urban areas or mountainous regions due to radar shadow and high backscatter. Despite these limitations, SAR-based validations consistently show high success ratios and low false alarm rates, although low POD in some events suggests model underestimation in capturing flooded areas. These results highlight SAR's value in verifying model performance.

4. The neighborhood verification method, using FSS, was applied to assess spatial consistency between 3Di simulations and SAR observations. Results show that increasing the neighborhood size improves FSS values, indicating better spatial agreement as local differences are smoothed. Events in Dongshan show higher FSS across all scales, likely due to the larger wetland coverage, while Kaohsiung events exhibit lower scores, suggesting more localized discrepancies. Overall, the method confirms acceptable spatial skill at native resolution and suggests potential benefits from higher-resolution validation datasets in the future. Nonetheless, SAR limitations in complex urban or vegetated environments remain a key challenge for accurate flood mapping.

5. To evaluate how the temporal resolution of precipitation data affects flood

modeling, this study compares QPESUMS10M and hourly QPESUMS datasets. Spatial analysis reveals discrepancies: QPESUMS10M often underestimates rainfall in Dongshan, while in Kaohsiung, it tends to overestimate. Scatter plots further confirm these patterns, especially under typhoon-influenced rainfall, where high variability is observed. Although overall precipitation differences between the two datasets are not extreme, flood simulations using QPESUMS10M consistently produce earlier and larger inundation areas. This indicates that higher temporal resolution enables better detection of short-term, intense rainfall and its hydrological impact, emphasizing its value in accurate flood forecasting and early warning systems.

6. To evaluate the performance of MAPLE's nowcasting system, we compared predicted rainfall fields which converted using a Z-R relationship with QPESUMS, and focusing on land-based precipitation. SCC analysis shows that MAPLE10mins consistently provides higher predictive skill across all events, with more time exceeding the SCC threshold of 0.5. In contrast, MAPLE60mins exhibits significantly weaker performance, with more low-correlation regions. In terms of error magnitude, RMSE analysis further supports this pattern, MAPLE10mins maintains the lowest errors across events, while MAPLE60mins shows the highest. Overall, the results suggest that MAPLE10mins offers more reliable precipitation predictions in Taiwan.

7. The performance of various precipitation inputs on flood simulation was assessed by comparing inundation areas generated by the 3Di model across different events. Simulation results show that MAPLE generally

underestimates flood extent, especially during intense rainfall events. However, the MAPLE10mins yields results closest to observations, effectively capturing flood trends and peak timing, highlighting the importance of high-frequency rainfall inputs.

8. Compared to larger basins, smaller basins like Dongshan are more sensitive to precipitation accuracy, where even minor forecast errors in rainfall fields can directly affect flood extent, emphasizing the need for precise spatial and temporal resolution. Although MAPLE struggles to capture localized convective systems and introduces some errors, its stable and smoothed rainfall input still offers value in flood simulations, particularly for operational forecasting scenarios.

Overall, the above results highlight the critical role of high-resolution precipitation data for accurate flood modeling and early warning. Results show that rainfall intensity distribution, temporal resolution, and nowcast accuracy significantly influence flood extent and timing. Validation using multiple data sources confirms the reliability of the 3Di model, though performance varies by region and data source. Among the strategies of QPE and nowcasts, high temporal resolution precipitation data consistently demonstrate higher and earlier inundation peaks in flood simulation, particularly in smaller, sensitive basins.

6.2 Future work

To enhance the accuracy and applicability of flood simulation and forecasting, several directions can be explored in future research. First, incorporating more diverse and higher-quality datasets can improve the model's

ability to capture real-world conditions. Extending the initial simulation period and accounting for soil saturation levels can help better represent the initial hydrological state of the system. Additionally, as tidal effects influence the drainage rate, integrating tidal data into the model could further refine simulation accuracy, especially in coastal or estuarine areas.

This study primarily focuses on typhoon-related events and northeasterly winds. Future work can expand the range of test cases to include different weather patterns, such as Mei-yu fronts or other frontal systems. Furthermore, applying the methodology across various geographical regions, including urban and rural areas of different scales, can help evaluate the generalizability of the model and assess the added value of high temporal resolution data under different environmental settings.

In addition to nowcasting systems like MAPLE, future studies may explore the performance of various numerical weather prediction (NWP) models, such as WRF, in simulating precipitation events at different temporal and spatial scales. Comparing deterministic and ensemble forecast outputs can help evaluate their suitability as inputs for flood modeling under diverse meteorological conditions.

Moreover, while this study primarily focuses on short-term rainfall forecasting and nowcasting applications, extending the forecasting horizon to medium- or long-range periods (e.g., 1–5 days) may offer valuable insights for early warning and preparedness. Such efforts would allow flood risk assessments under more uncertain but proactive scenarios, contributing to the development of an integrated, multi-scale flood forecasting system.

Reference

Alfieri, L., P. Salamon, F. Pappenberger, F. Wetterhall, and J. Thielen, 2012: Operational early warning systems for water-related hazards in Europe. *Environmental Science & Policy*, **21**, 35–49.

Bellon, A., I. Zawadzki, A. Kilambi, H. C. Lee, Y. H. Lee, and G. Lee, 2010: McGill algorithm for precipitation nowcasting by lagrangian extrapolation (MAPLE) applied to the South Korean radar network. Part I: Sensitivity studies of the Variational Echo Tracking (VET) technique. *Asia-Pacific Journal of Atmospheric Sciences*, **46**, 369–381.

Cloke, H. L., and F. Pappenberger, 2009: Ensemble flood forecasting: A review. *Journal of Hydrology*, **375**, 613–626.

Chang, C.-H., Rahmad, R., Wu, S.-J., Hsu, C.-T., & Chung, P.-H. (2024). Enhancing flood verification using Signal Detection Theory (SDT) and IoT Sensors: A spatial scale evaluation. *Journal of Hydrology*, *636*, 131308.

Chang, P.-L., and Coauthors, 2020: An operational Multi-Radar Multi-Sensor QPE system in Taiwan. *Bulletin of the American Meteorological Society*, **102**, E555–E577.

Chung, K.-S., and I.-A. Yao, 2019: Improving Radar Echo Lagrangian Extrapolation Nowcasting by blending numerical model wind information: Statistical performance of 16 typhoon cases. *Monthly Weather Review*, **148**, 1099–1120.

Emmanuel, I., H. Andrieu, E. Leblois, and B. Flahaut, 2012: Temporal and spatial variability of rainfall at the urban hydrological scale. *Journal of Hydrology*, **430–431**, 162–172.

Germann, U., and I. Zawadzki, 2002: Scale-Dependence of the Predictability of Precipitation from Continental Radar Images. Part I: Description of the Methodology. *Monthly Weather Review*, **130**, 2859–2873.

Germann, U., I. Zawadzki, and B. Turner, 2006: Predictability of Precipitation from Continental Radar Images. Part IV: Limits to Prediction. *J. Atmos. Sci.*, **63,** 2092-2108.

Grimaldi, S., Y. Li, V. R. N. Pauwels, and J. P. Walker, 2016: Remote Sensing-Derived Water Extent and Level to Constrain Hydraulic Flood Forecasting Models: Opportunities and Challenges. *Surveys in Geophysics*, **37**, 977–1034.

Hooker, H., S. L. Dance, D. C. Mason, J. Bevington, and K. Shelton, 2022: Spatial scale evaluation of forecast flood inundation maps. *Journal of Hydrology*, **612**, 128170.

Hsu, Y.-C., G. Prinsen, L. Bouaziz, Y.-J. Lin, and R. Dahm, 2016: An investigation of DEM resolution influence on flood inundation simulation. *Procedia Engineering*, **154**, 826–834.

Laroche, S., and I. Zawadzki, 1994: A Variational Analysis Method for Retrieval of Three-Dimensional Wind Field from Single-Doppler Radar Data. *J. Atmos. Sci.*, **51,** 2664-2682.

Lawrence, J., A. Reisinger, B. Mullan, and B. Jackson, 2013: Exploring climate change uncertainties to support adaptive management of changing flood-risk. *Environmental Science & Policy*, **33**, 133–142.

Lee, H. C., Y. H. Lee, J.-C. Ha, D.-E. Chang, A. Bellon, I. Zawadzki, and G. Lee, 2010: McGill algorithm for precipitation nowcasting by lagrangian extrapolation (MAPLE) applied to the South Korean radar network. Part II: Real-time verification for the summer season. *Asia-Pacific Journal of Atmospheric Sciences*, **46**, 383–391.

Mandapaka, P. V., U. Germann, L. Panziera, and A. Hering, 2011: Can Lagrangian Extrapolation of Radar Fields Be Used for Precipitation Nowcasting over Complex Alpine Orography? *Weather and Forecasting*, **27**, 28–49.

Ochoa-Rodriguez, S., and Coauthors, 2015: Impact of spatial and temporal resolution of rainfall inputs on urban hydrodynamic modelling outputs: A multi-catchment investigation. *Journal of Hydrology*, **531**, 389–407.

Pan, J.-W., K.-S. Chung, H.-H. Lin, T.-C. C. Wang, and I.-A. Yao, 2018: Feasibility Assessment of Applying Variational Radar Echo Tracking Method over Complex Terrain in Taiwan. *Atmospheric Sciences*, **46,** 1-34.

Papaioannou, G., L. Vasiliades, A. Loukas, and G. T. Aronica, 2017: Probabilistic flood inundation mapping at ungauged streams due to roughness coefficient uncertainty in hydraulic modelling. *Advances in Geosciences*, **44**, 23–34.

Roberts, N. M., and H. W. Lean, 2008: Scale-Selective Verification of Rainfall Accumulations from High-Resolution Forecasts of Convective Events. *Monthly Weather Review*, **136**, 78–97.

Roebber, P. J., 2008: Visualizing multiple measures of forecast quality. *Weather and Forecasting*, **24**, 601–608.

Saadi, M., C. Furusho-Percot, A. Belleflamme, S. Trömel, S. Kollet, and R. Reinoso-Rondinel, 2023: Comparison of three Radar-Based precipitation nowcasts for the extreme July 2021 flooding event in Germany. *Journal of Hydrometeorology*, **24**, 1241–1261.

Schumann, G., P. D. Bates, M. S. Horritt, P. Matgen, and F. Pappenberger, 2009: Progress in integration of remote sensing–derived flood extent and stage data and hydraulic models. *Reviews of Geophysics*, **47**.

Stelling, G. S., 2012: Quadtree flood simulations with sub-grid digital elevation models. *Proceedings of the Institution of Civil Engineers - Water Management*, **165**, 567–580.

Trenberth, K., 2010: Changes in precipitation with climate change. *Climate Research*, **47**, 123–138.

Turner, B. J., I. Zawadzki, and U. Germann, 2004: Predictability of Precipitation from Continental Radar Images. Part III: Operational Nowcasting Implementation (MAPLE). *Journal of Applied Meteorology*, **43**, 231–248.

Wing, O. E. J., P. D. Bates, C. C. Sampson, A. M. Smith, K. A. Johnson, and T. A. Erickson, 2017: Validation of a 30 m resolution flood hazard model of the conterminous United States. *Water Resources Research*, **53**, 7968–7986.

Zwiers, F. W., and Coauthors, 2013: Climate Extremes: Challenges in estimating and understanding recent changes in the frequency and intensity of extreme climate and weather events. *Springer eBooks*, 339–389.

Nelen & Schuurmans. (n.d.). *3Di documentation*. Retrieved April 21, 2025, from https://docs.3di.live/

陳如瑜, 張偉裕, and 陳台琦, 2017: 北台灣 S 與 C 波段雙偏極化雷達定量降雨估計之比較. *大氣科學*, **45**, 57-81.

邱俊穎, 謝嘉聲, 黃宗仁, 葉堃生, 管立豪, & 胡植慶. (2019). 合成孔徑雷達影像於颱風豪雨後淹水之偵測. *航測及遙測學刊*, *24*(4), 211-222.

許育蕎。利用三維回波移動場改善即時降雨預報並建構系集即時預報系統：臺灣梅雨鋒面及秋季降水個案分析。碩士論文，國立中央大學，民國 112 年 6 月。

賴茂修。應用洪災指標於二維 HEC-RAS 及 3Di 模式之評估。碩士論文，國立臺灣大學，民國 111 年 8 月。

Table

Table 1. The list of selected events.

	NAME	START TIME	SIMULATION HOURS	LOCATION
Case1	Typhoon Gaemi	2024/07/24 04UTC	24	Dongshan
Case2	Typhoon Krathon	2024/10/03 08UTC	12	Dongshan
Case3	Typhoon Trami and Northeasterly	2024/10/24 04UTC	24	Dongshan
Case4	Northeasterly and Typhoon Toraji	2024/11/12 04UTC	24	Dongshan
Case5	Typhoon Gaemi	2024/07/24 12UTC	24	Kaohsiung
Case6	Typhoon Krathon	2024/10/03 00UTC	12	Kaohsiung

Table 2. The parameters setting of 3Di.

Model	Dongshan	Kaohsiung
Area (km^2)	112.728	939.473
DEM (m)	1	1
Simulation time step	10s	10s
Output time step	300s	300s

Table 3. The VET setting of MAPLE

VET parameter	**setting**
Number of maps	3
Time difference between each map	20
Amount of smoothing	3×3
Reflectivity threshold	5
Number of scaling guesses	5
Vector density of scaling guesses	144×144
Relative weightings for $\beta$and γ	0.5 and 1000

Table 4. The data availability in different cases.

Data	**20180823 Kaohsiung**	**20240724 Dongshan**	**20240724 Kaohsiung**	**20241003 Dongshan**	**20241003 Kaohsiung**	**20241024 Dongshan**	**20241112 Dongshan**
EMIC							
Flood sensor							
SAR							

Table 5 Four categories of the confusion matrix

Observed / Forecast	$O \geq$ Threshold	$O <$ Threshold
$F \geq$ Threshold	Hit(a)	False alarm(c)
$F <$ Threshold	Miss(b)	Correct negative(d)

Table 6. The number of EMIC in the selected events.

Events	EMIC records
2024-07-24, Dongshan	7
2024-10-03, Dongshan	26
2024-10-24, Dongshan	0
2024-11-12, Dongshan	0
2018-08-23, Kaohsiung	686
2024-07-24, Kaohsiung	1183
2024-10-03, Kaohsiung	294

Table 7. The number of detections and detection rate by 3Di.

Events	EMIC records	The number of detections	Detection rate
2018-08-23, Kaohsiung	686	549	80%
2024-07-24, Kaohsiung	1183	1129	95%
2024-10-03, Kaohsiung	294	235	80%

Figure

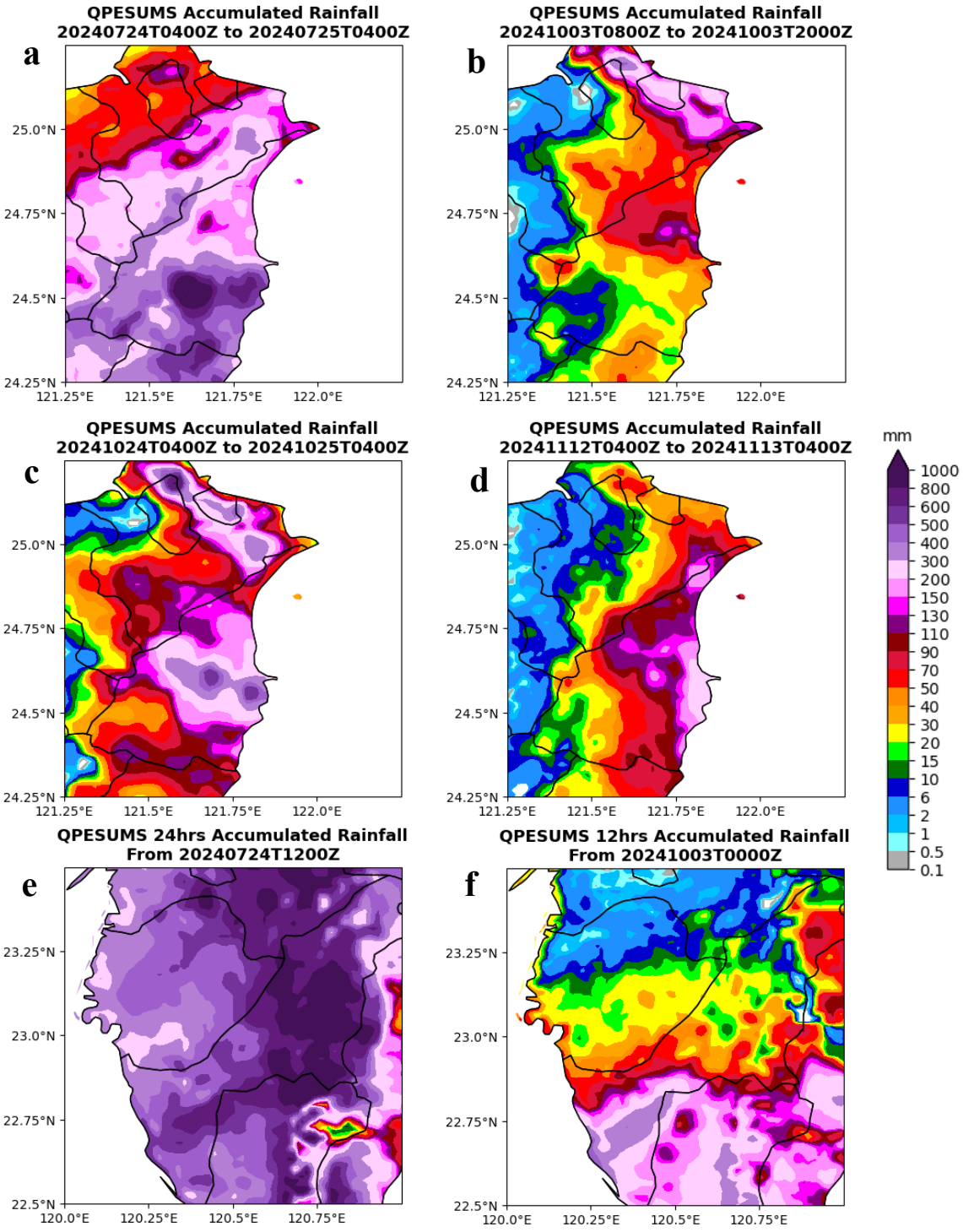

Figure 1. Accumulated rainfall during flood simulation time in six cases.

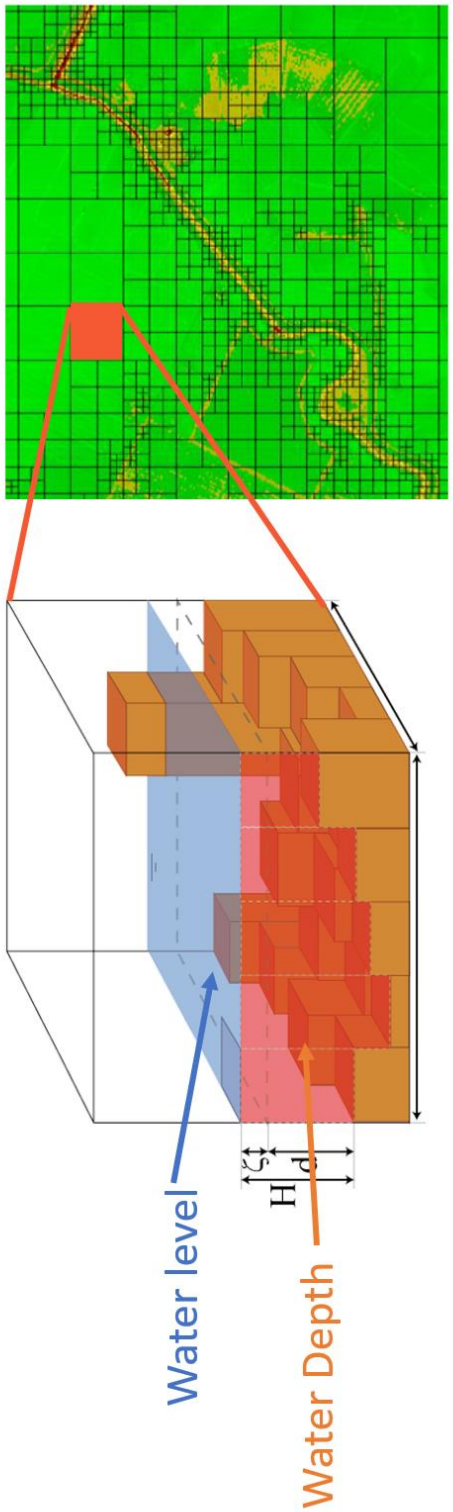

Figure 2. An illustration of a computational cell using quad-tree refinements and a water depth defined on the sub-grid. (adopted from 3Di documentation).

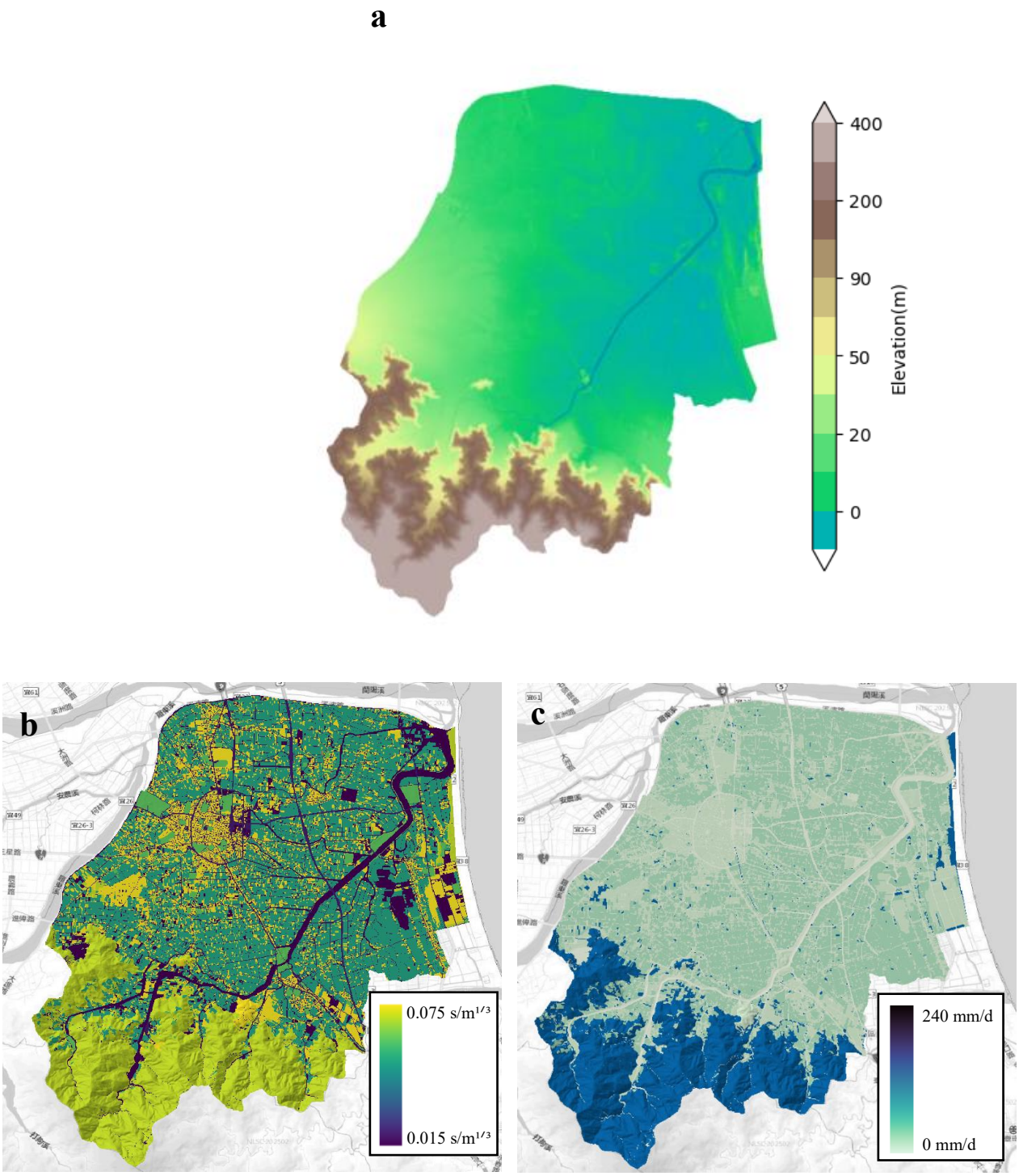

Figure 3. Basic information of Dongshan used in the 3Di model. (a) The DEM. (b) roughness map. (c) Infiltration map.

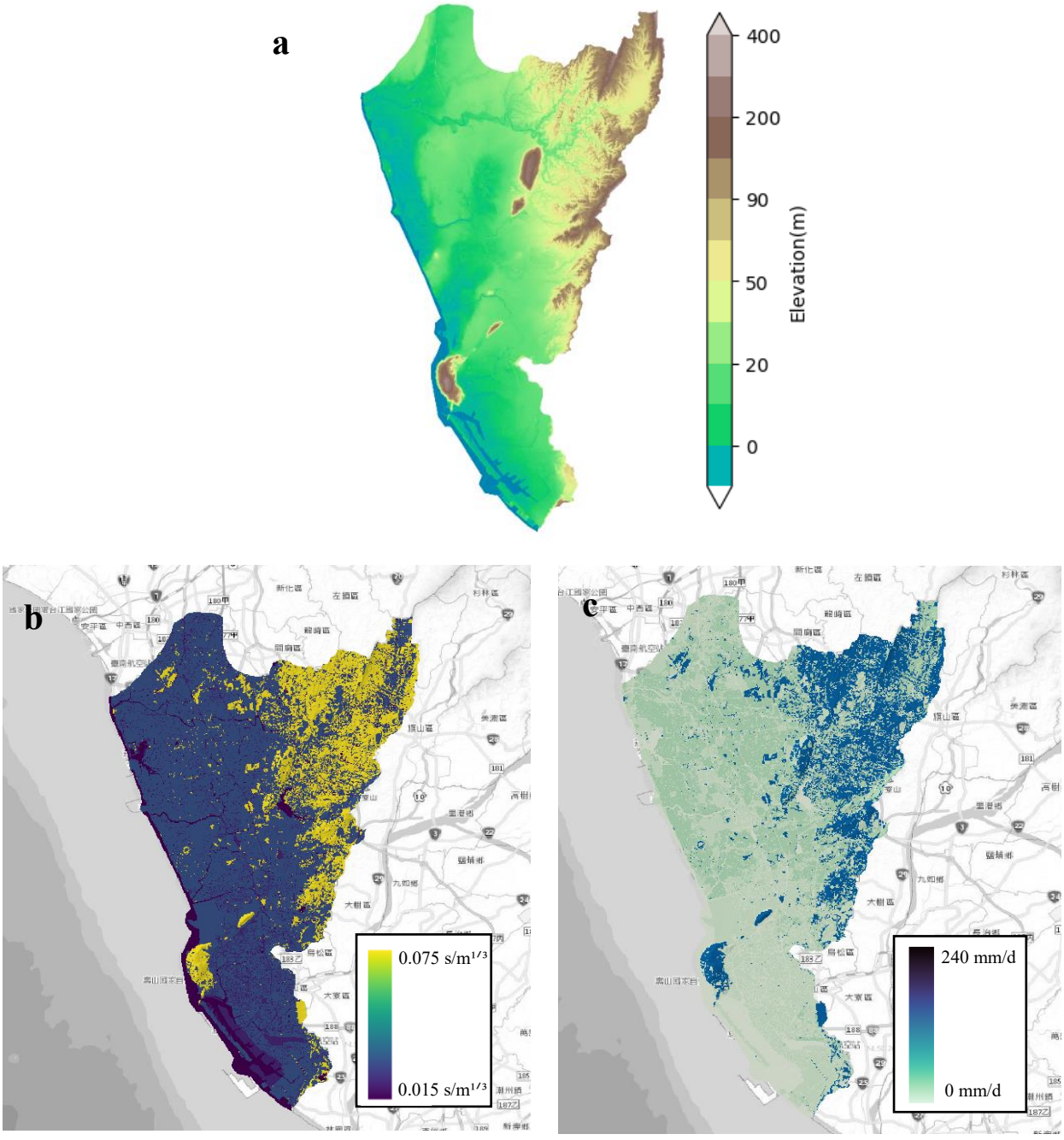

Figure 4. Basic information of Kaohsiung used in the 3Di model. (a) The DEM. (b) roughness map. (c) Infiltration map.

b

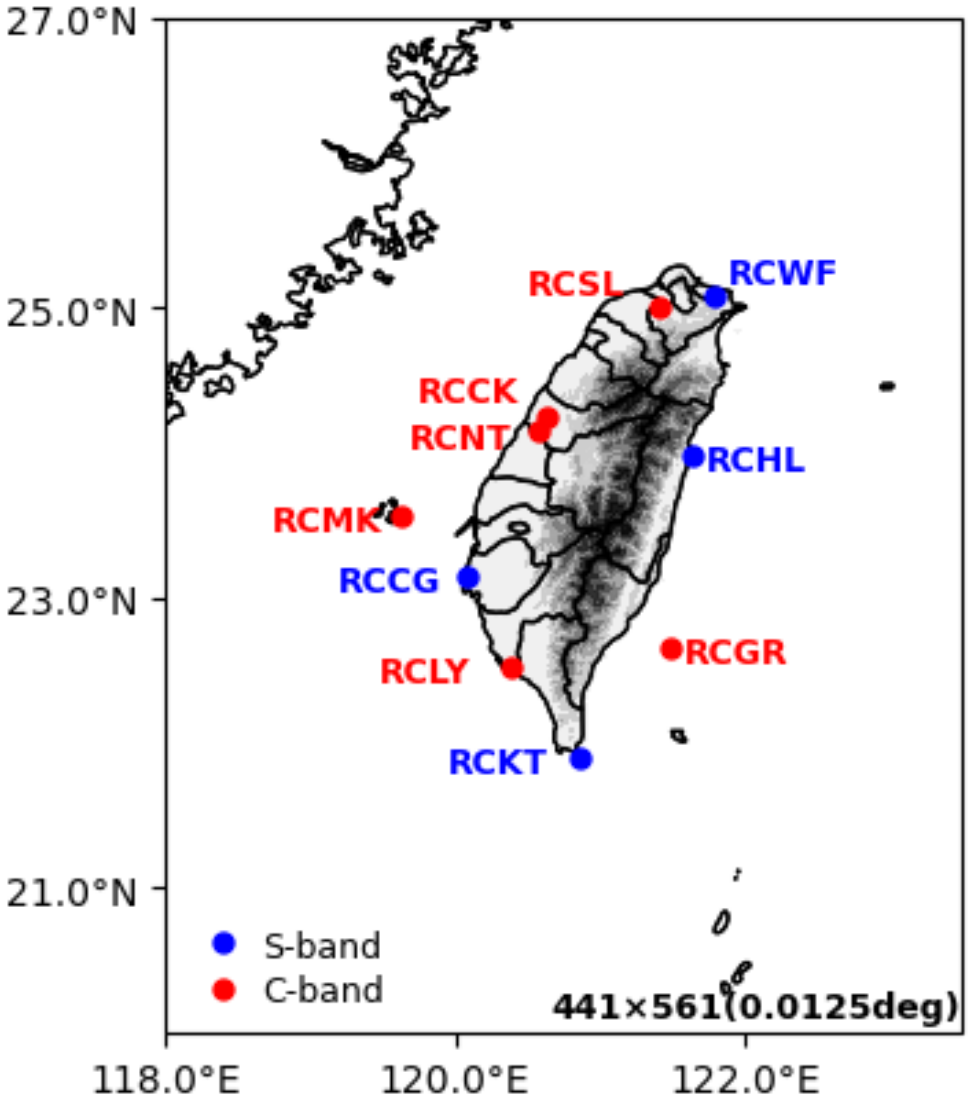

Figure 5. The positions of radars in Taiwan. Red dots are C-band radars, blue dots are S-band radars.

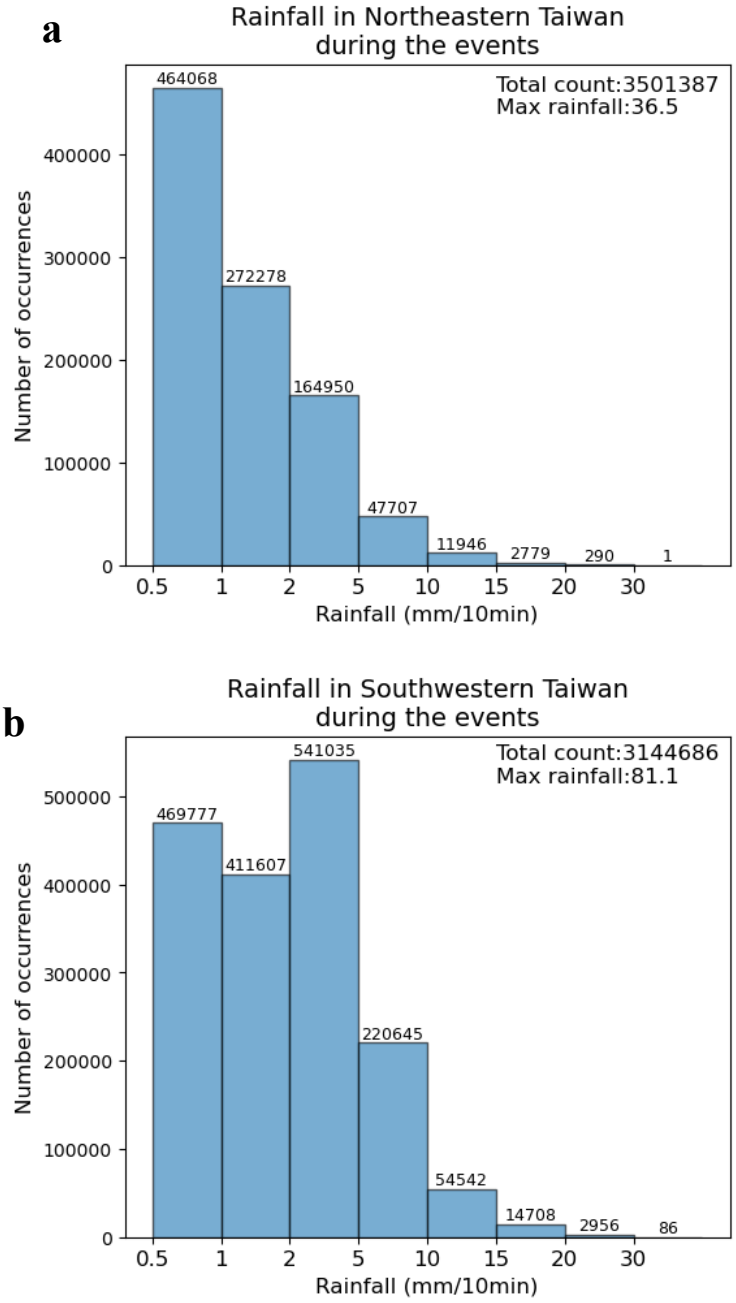

Figure 6. The distribution of rainfall intensity during significant rainfall events in (a) Northeastern and (b) Southwestern Taiwan.

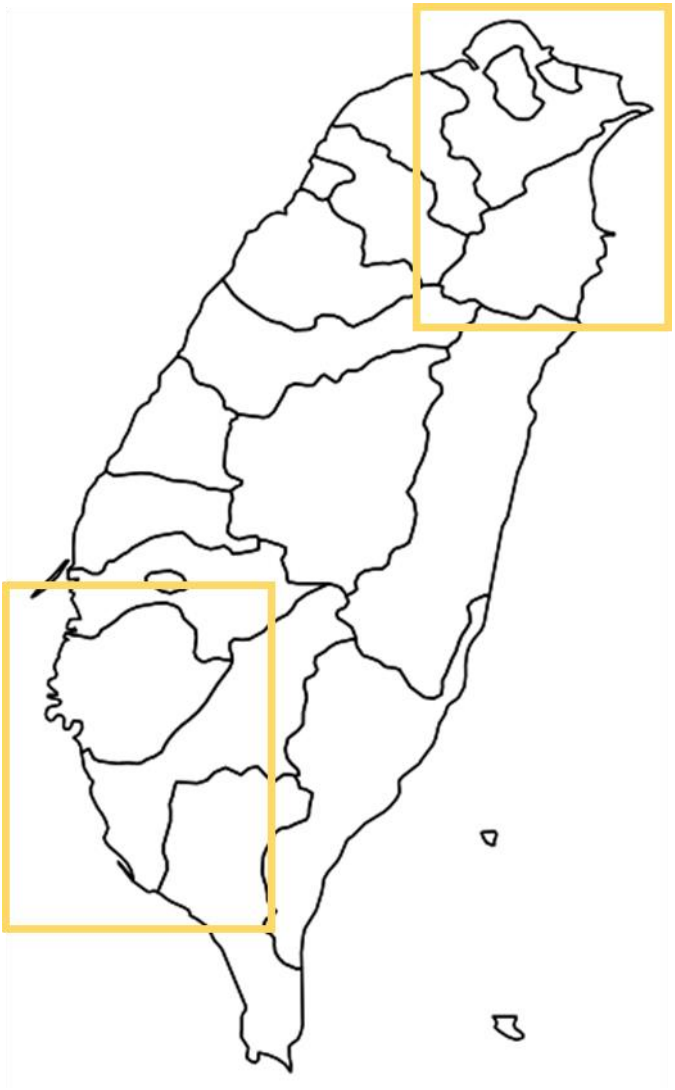

Figure 7. The calculated 9 area of Figure 6

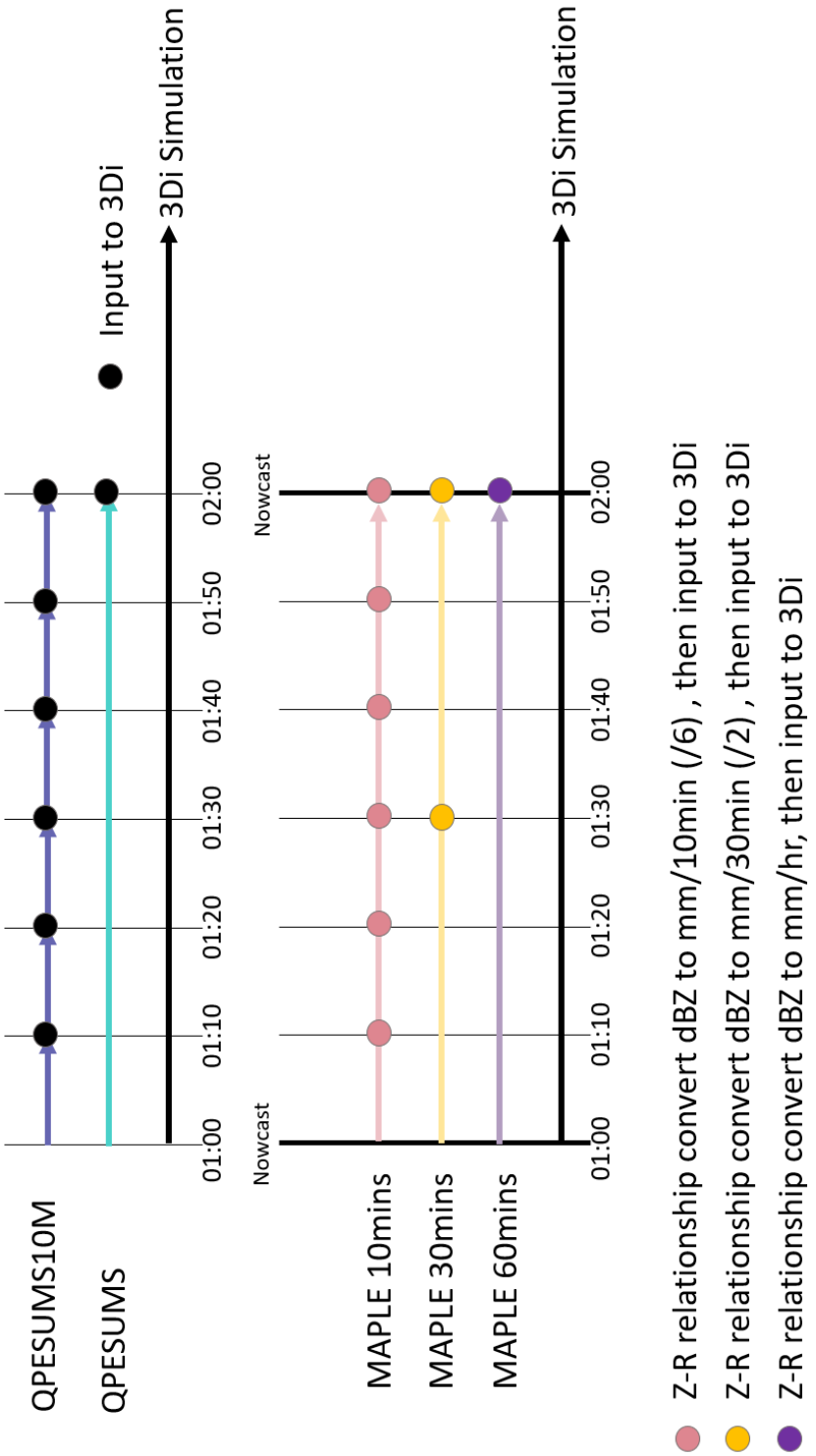

Figure 8. Experiment setting in this study.

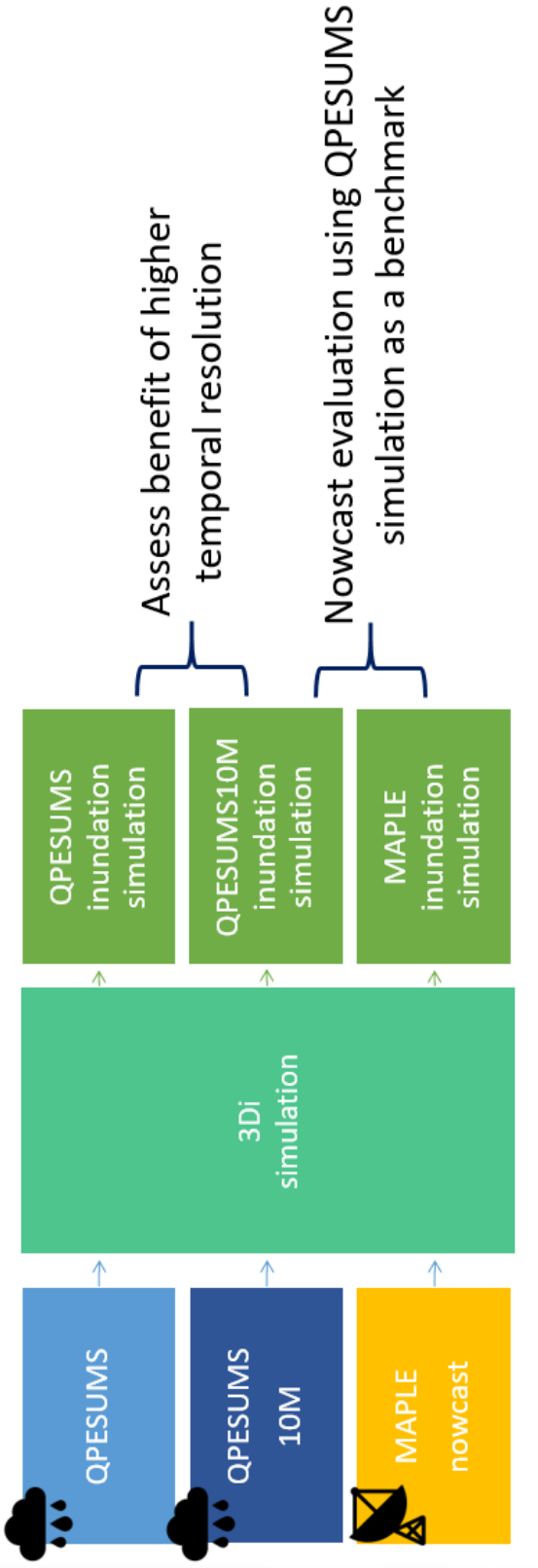

Figure 9. The overall workflow of the inundation simulations.

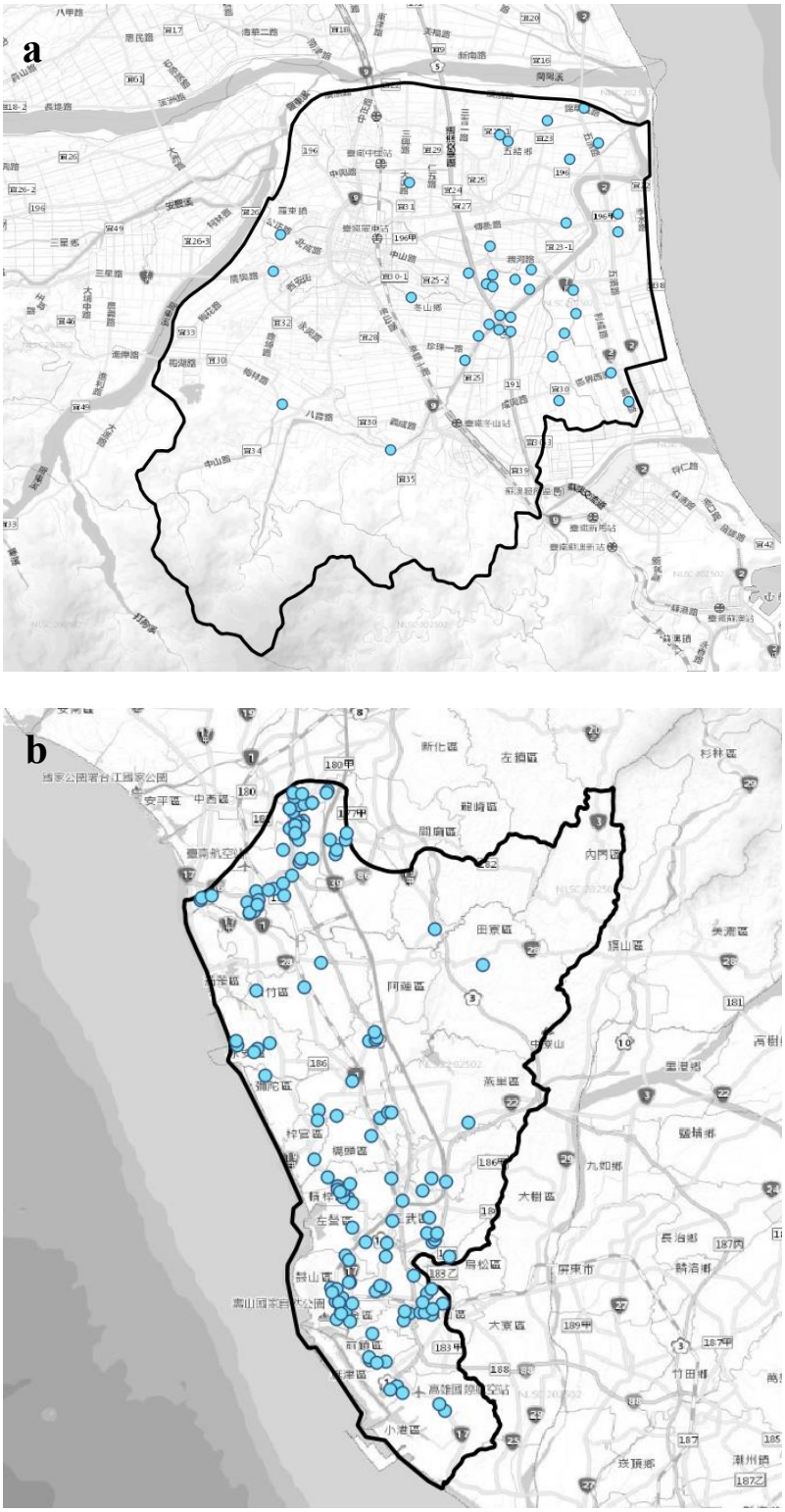

Figure 10. The locations of flood sensors in (a) Dongshan and (b) Kaohsiung.

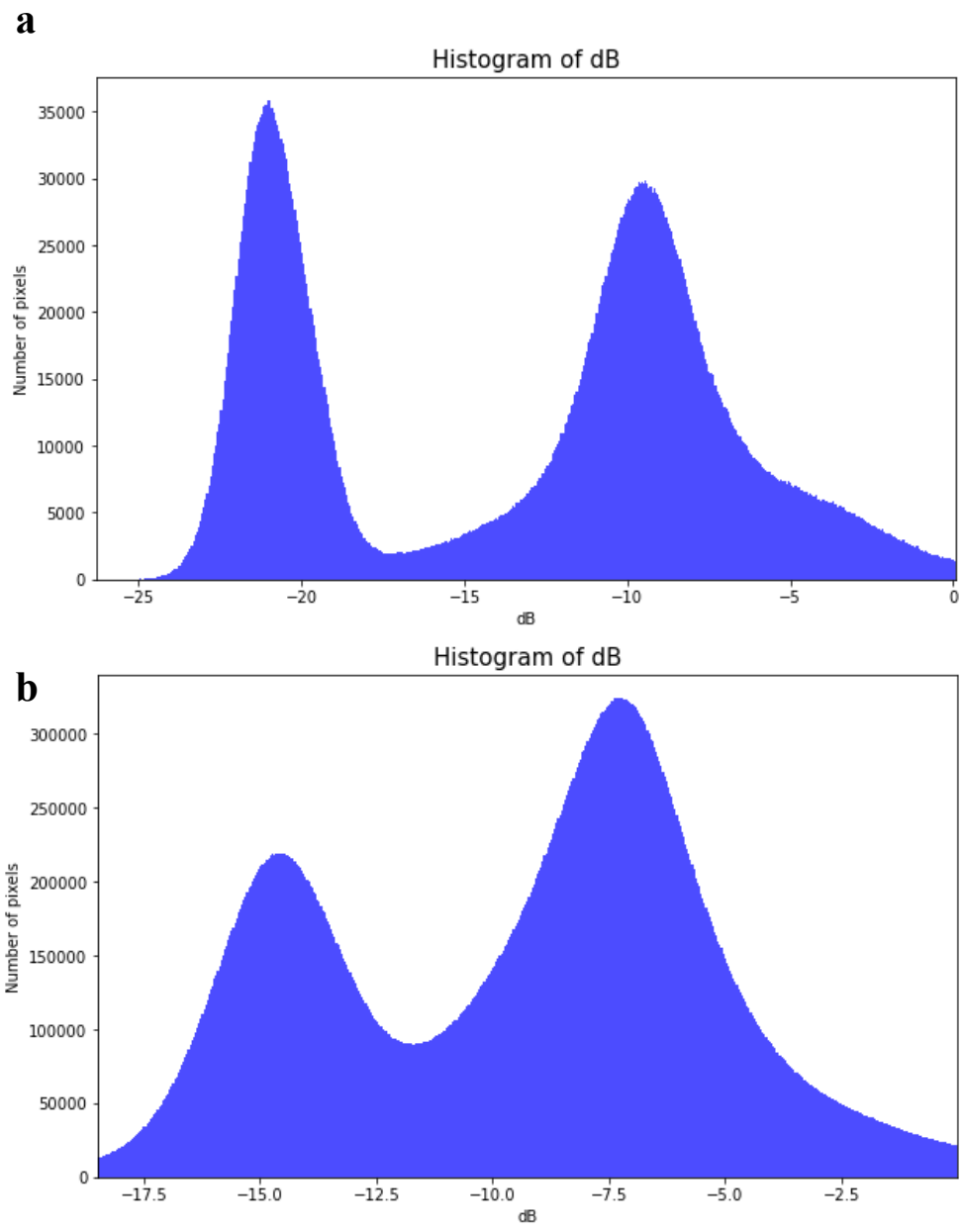

Figure 11. Histogram analysis based on SAR images in (a) northeastern and (b) southwestern Taiwan.

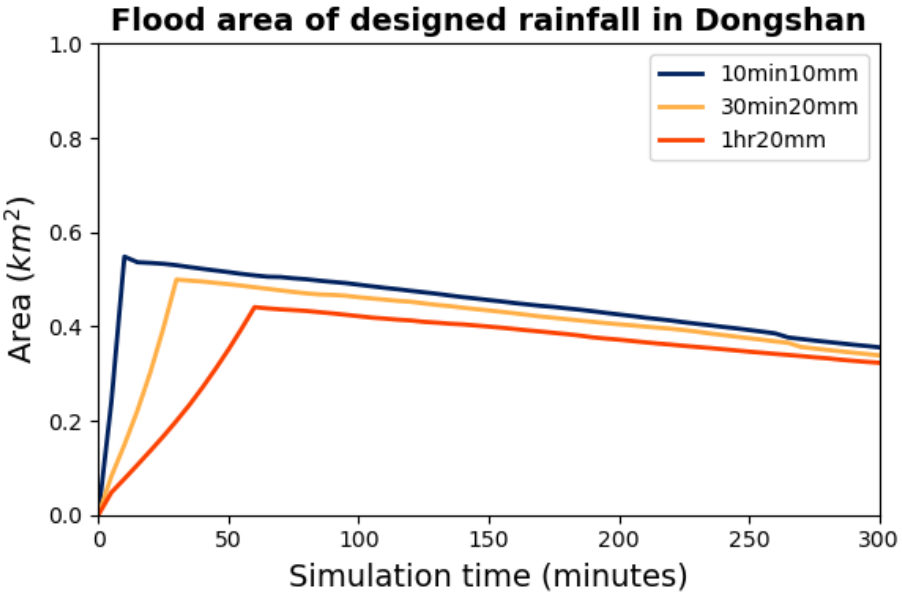

Figure 12. The flood area of the 3 scenarios with a total precipitation 20 mm.

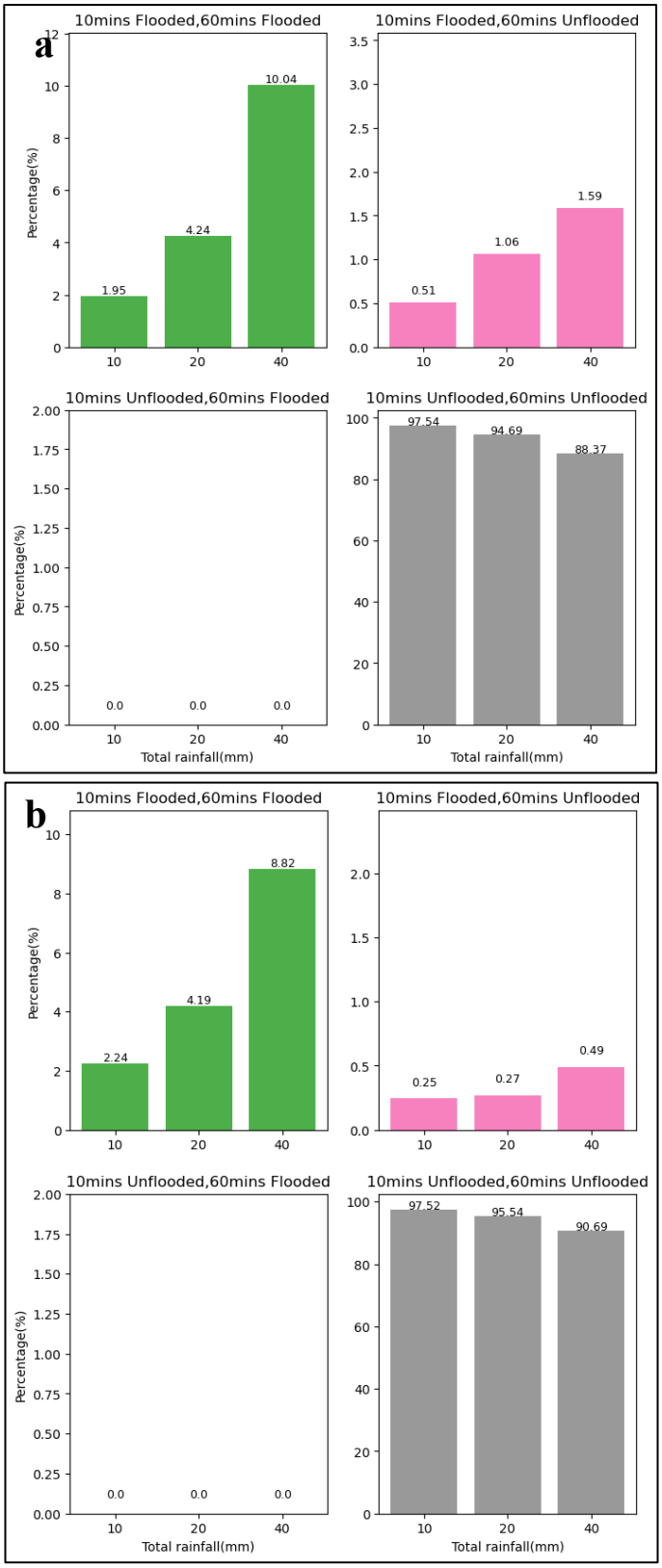

Figure 13. The percentage of flooded and unflooded areas under two different rainfall distributions. (a) Dongshan. (b) Kaohsiung.

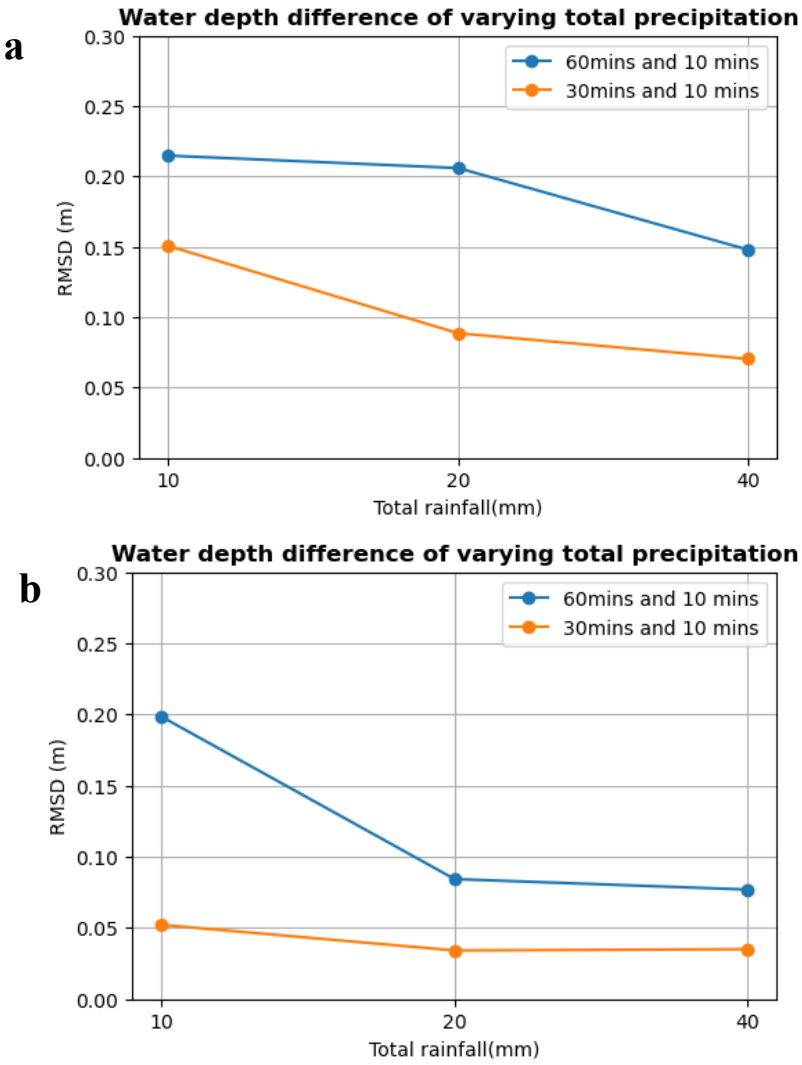

Figure 14. Water depth difference of varying precipitation amount. (a) Dongshan. (b) Kaohsiung.

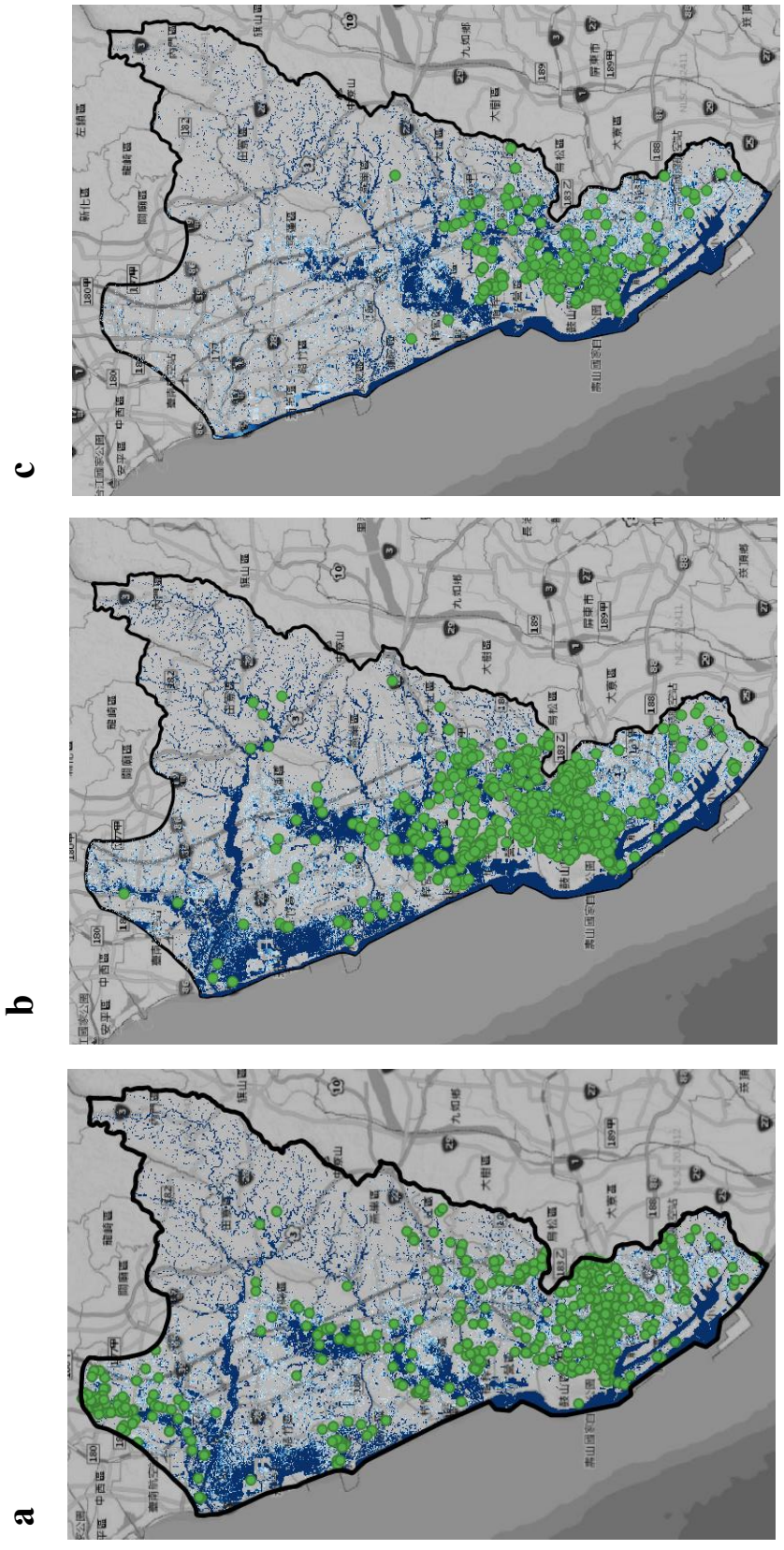

Figure 15. The distribution of EMIC and the maximum water depth simulated by 3Di in the events. (a) 2018-08-23 (b) 2024-07-24 (c) 2024-10-03

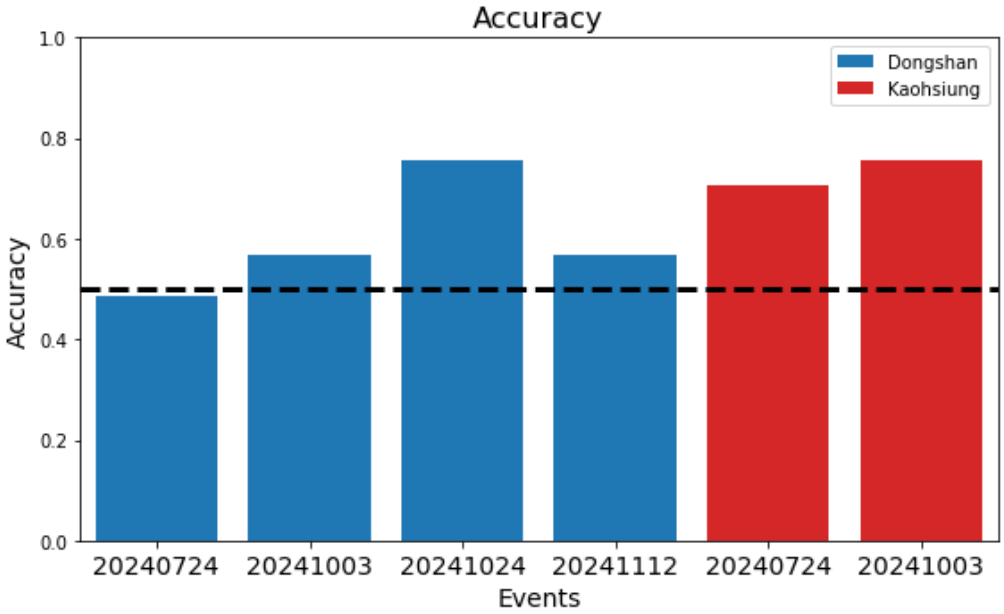

Figure 16. Accuracy compared with flood sensors.

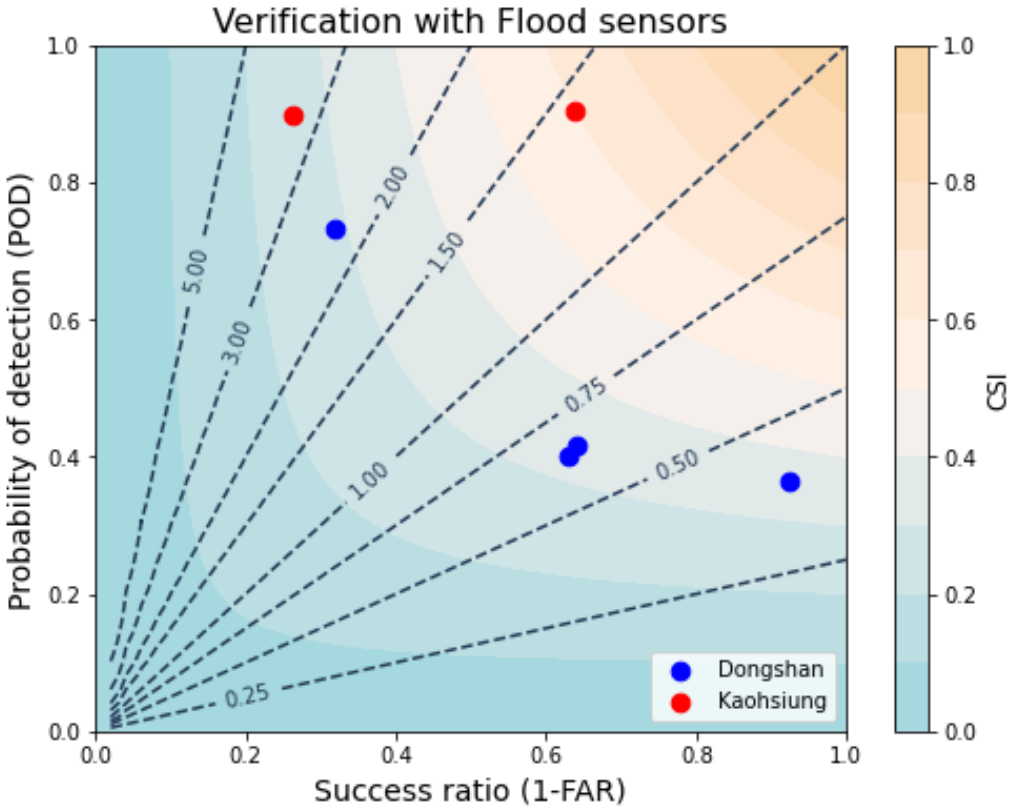

Figure 17. Performance diagram, flood sensors used as reference.

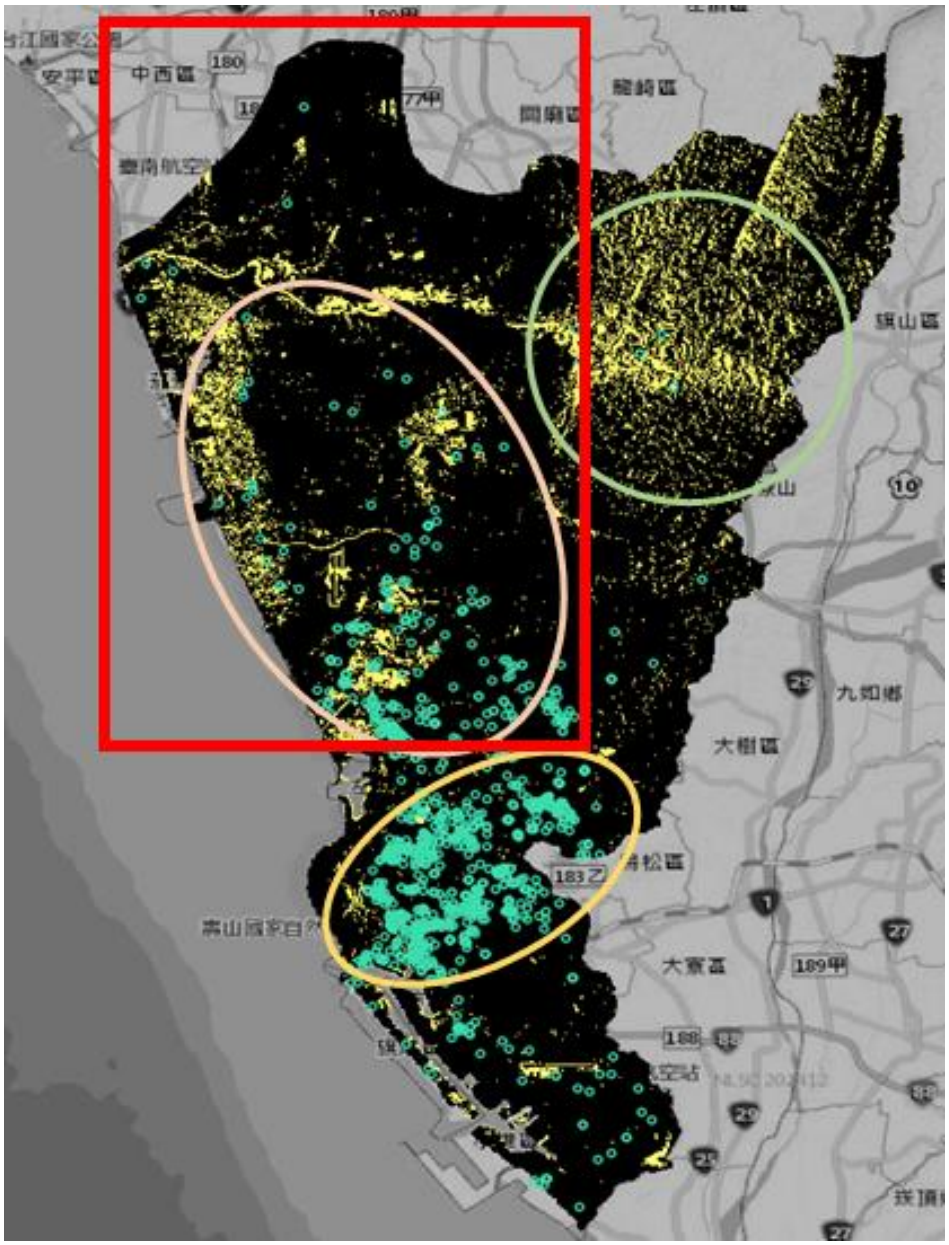

Figure 18. Water area detected by SAR and the distribution of EMIC. Light-green circle is effected by terrain. Yellow circle is the main urban area. Pink circle shows a good match of SAR detection and EMIC, therefore, Red box shows the calculated regions of verification.

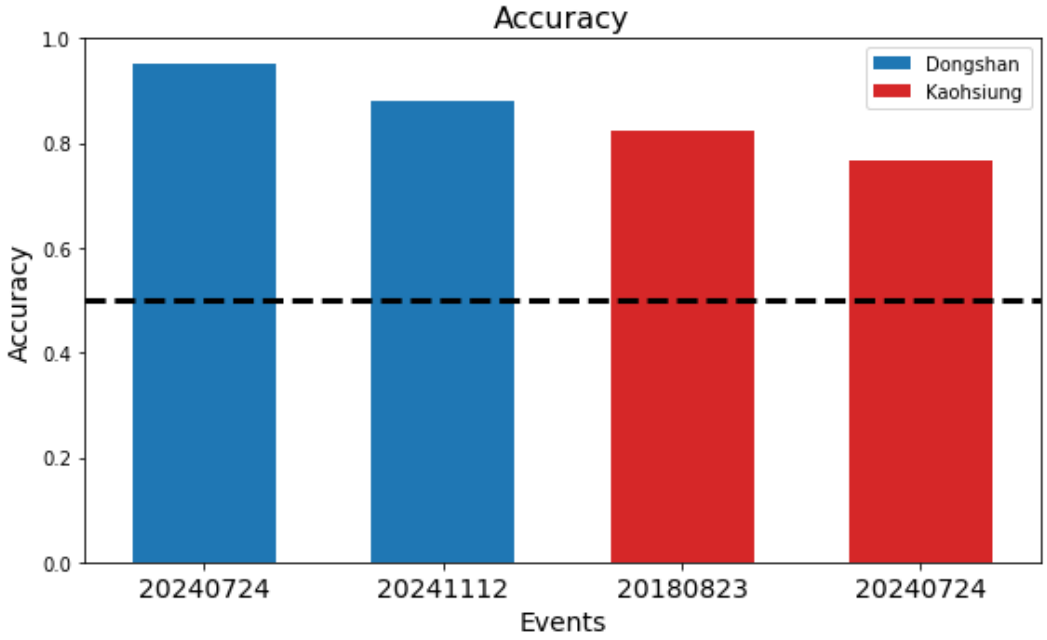

Figure 19. Accuracy compared with SAR images.

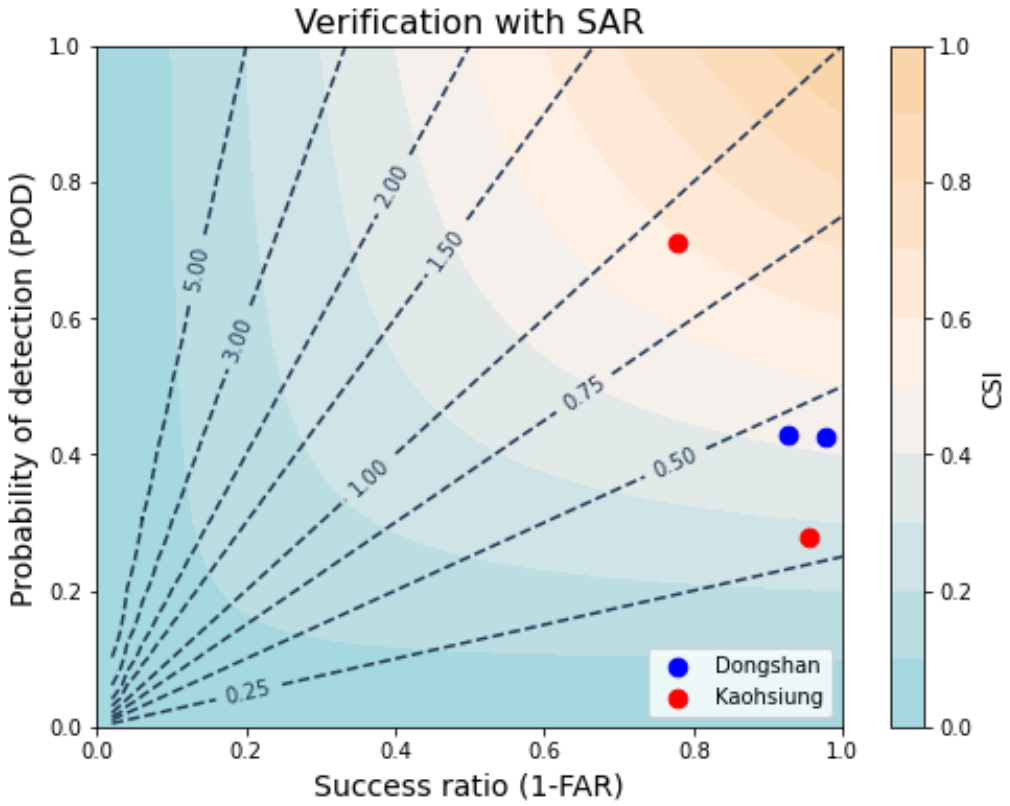

Figure 20. Performance diagram, SAR data used as reference.

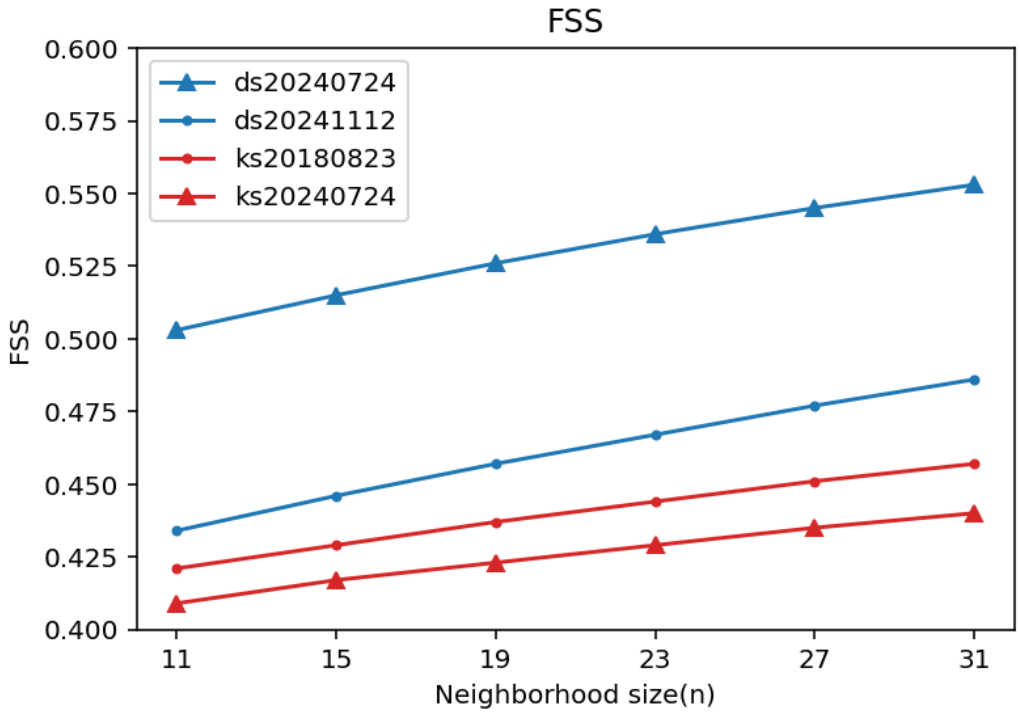

Figure 21. FSS score with neighborhood size from 11 to 31.

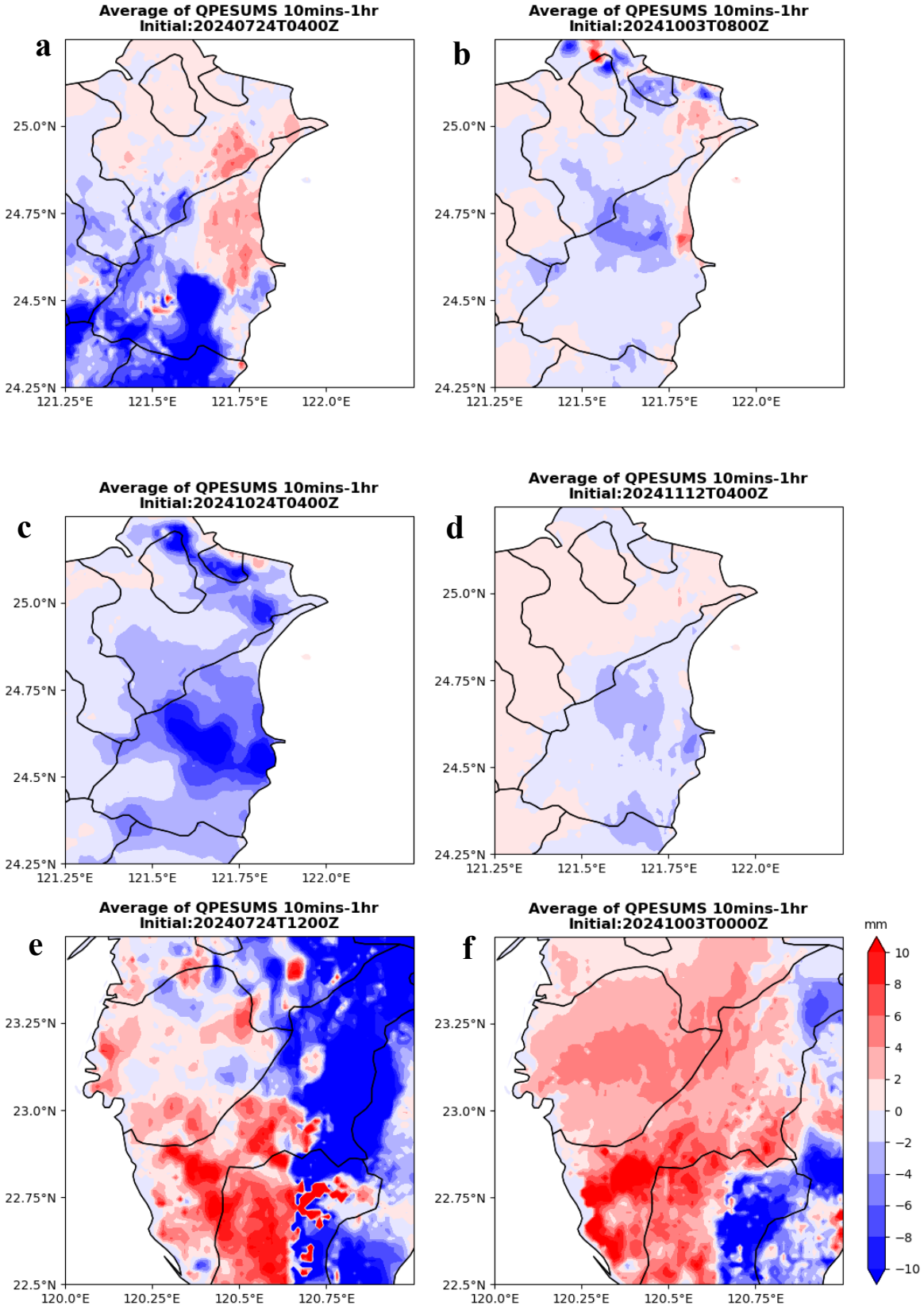

Figure 22. The hourly average difference of QPESUMS10M and QPESUMS

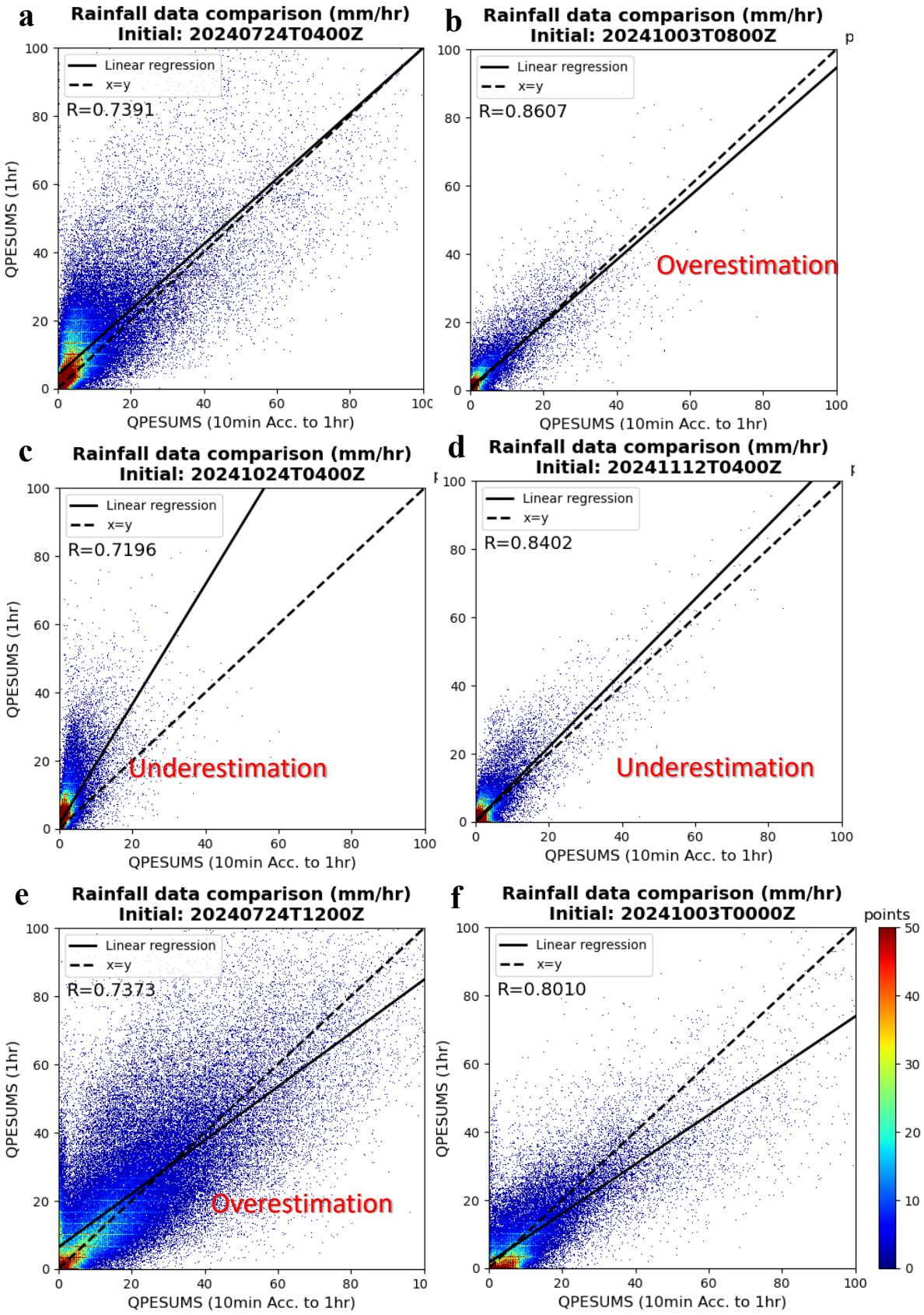

Figure 23. The scatter plot of QPESUMS10M sum up to 1 hour and QPESUMS.

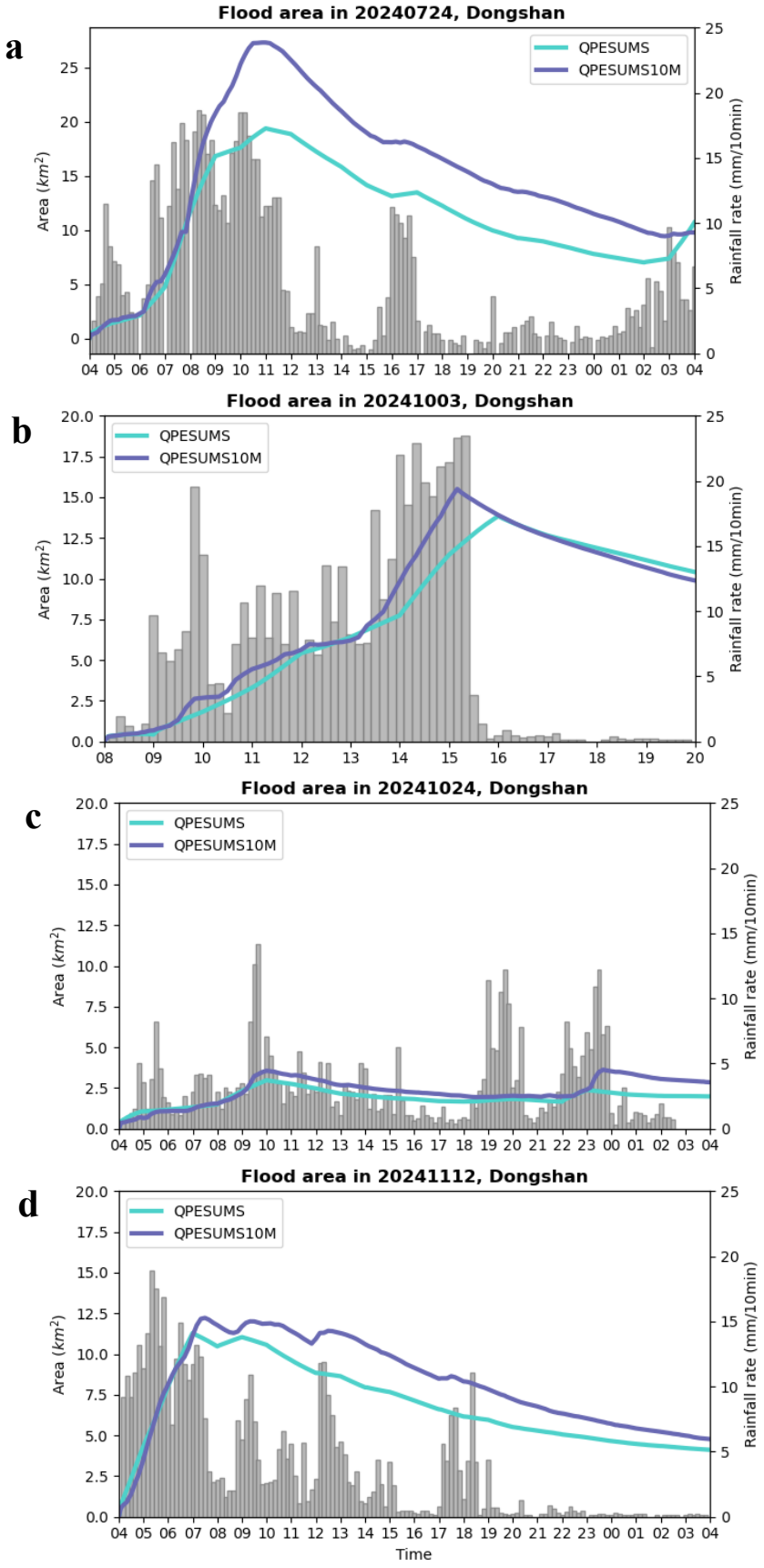

Figure 24. The flood area using QPESUMS10M and QPESUMS. The gray bar is the maximum 10-minute rainfall in the basin.

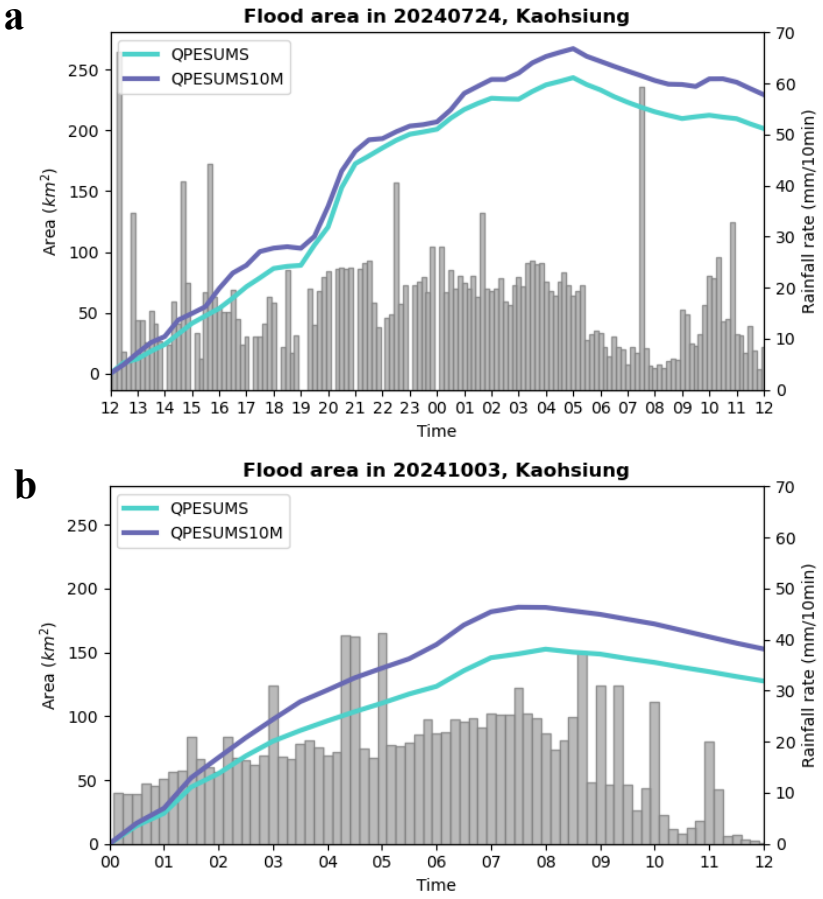

Figure 25. The flood area using QPESUMS10M and QPESUMS. The gray bar is the maximum 10 minute rainfall in the basin.

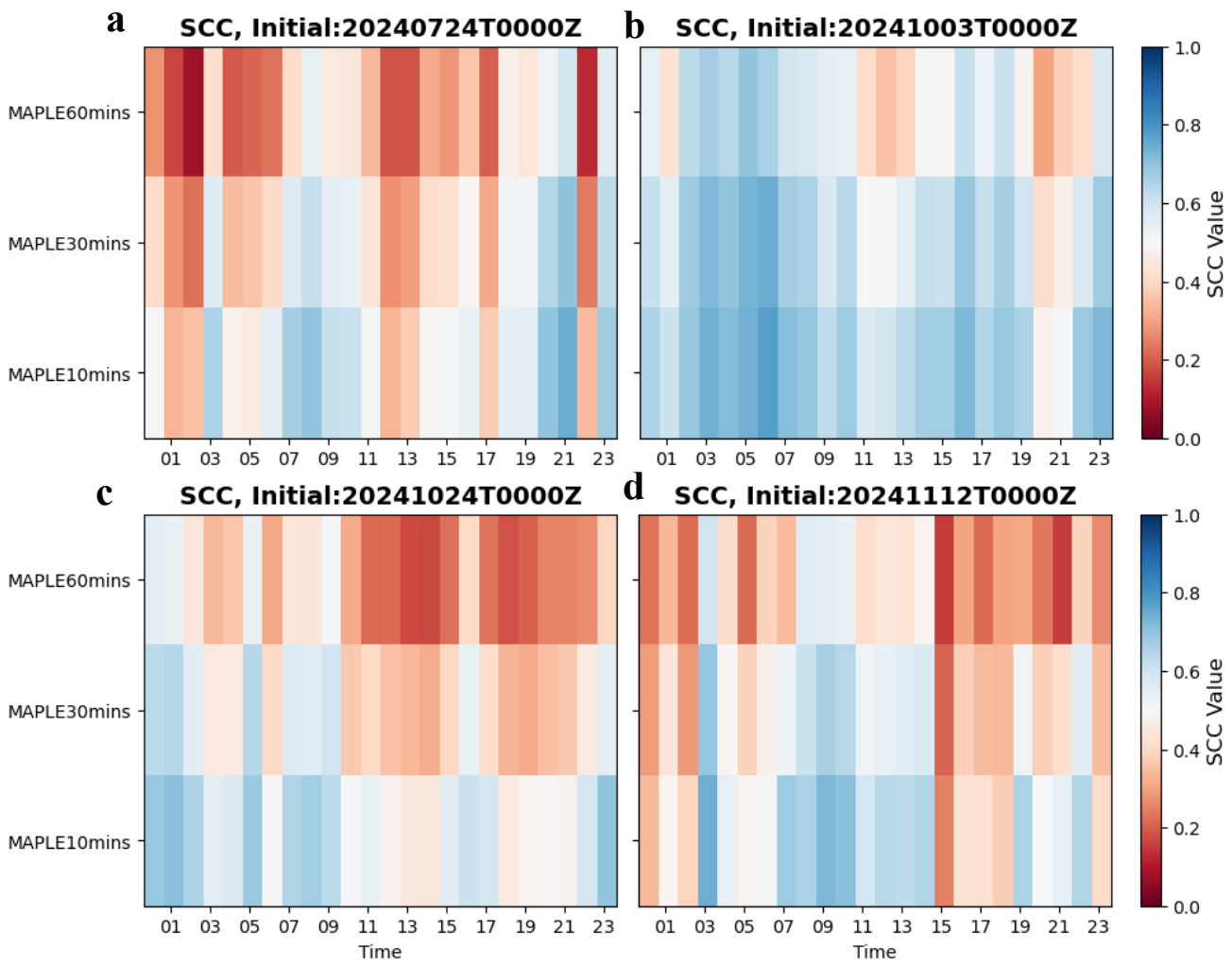

Figure 26. Heat map of SCC evolution.

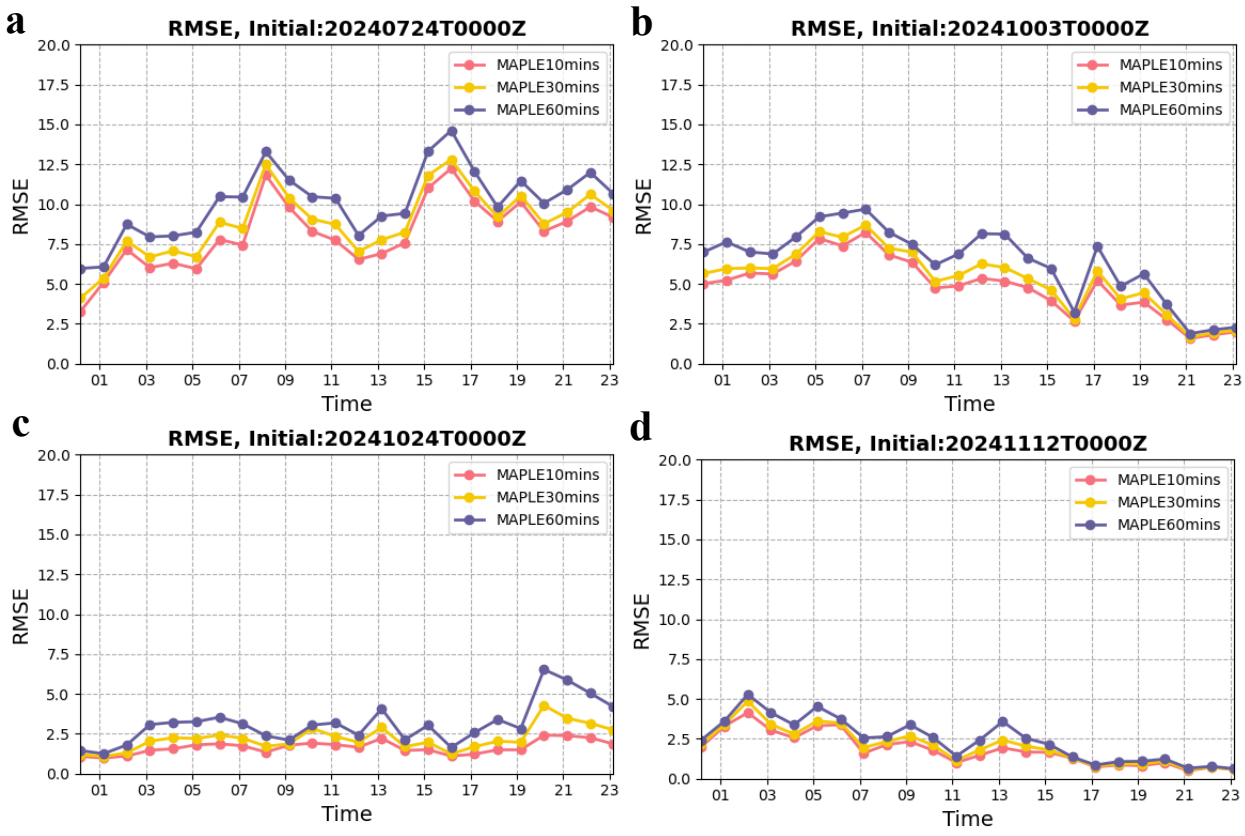

Figure 27. RMSE evolution.

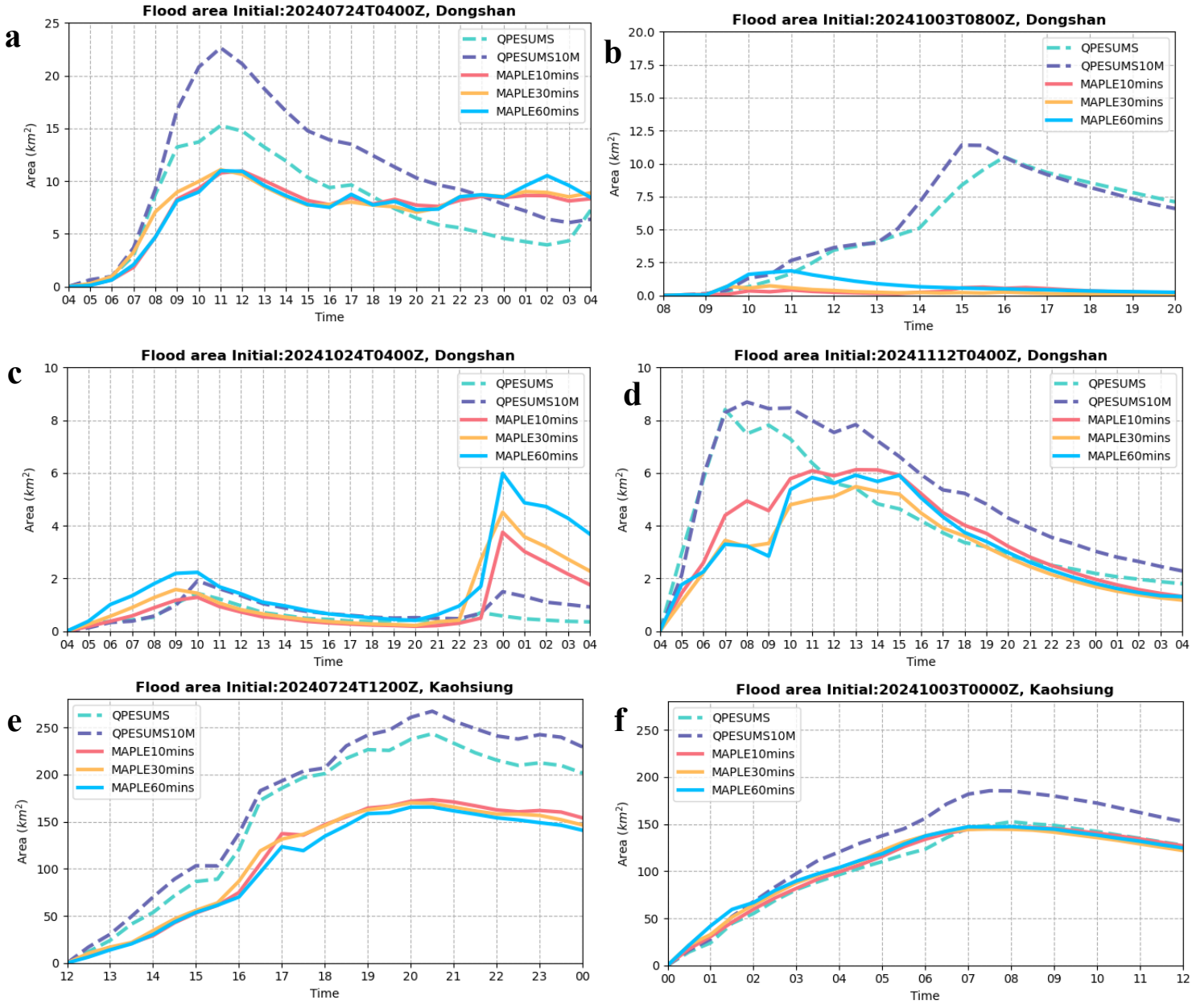

Figure 28. The inundation area across events.

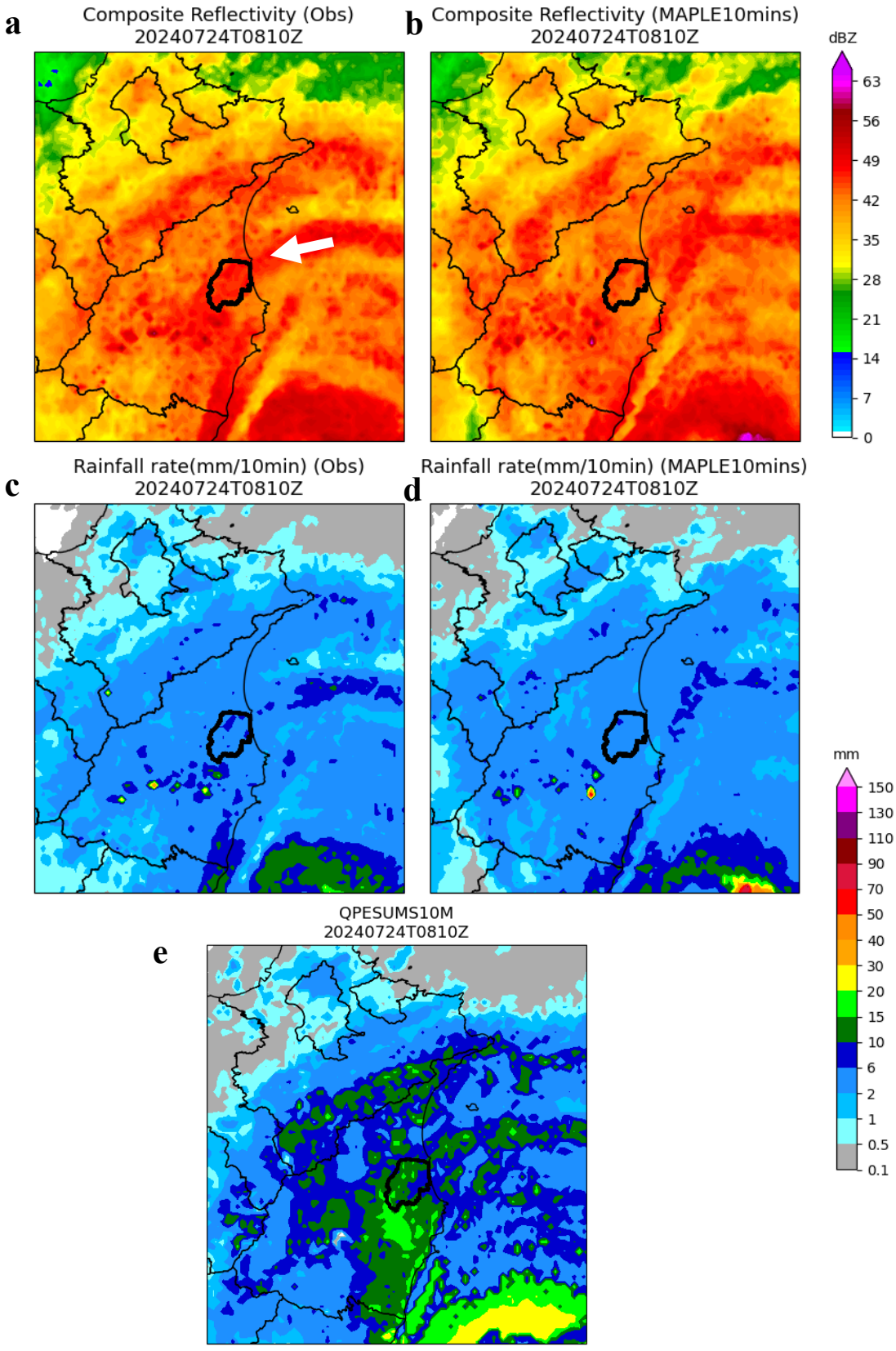

Figure 29. Observed and MAPLE forecast reflectivity, and convert to rainfall field by the Z-R relationship in the event 2024-07-24.

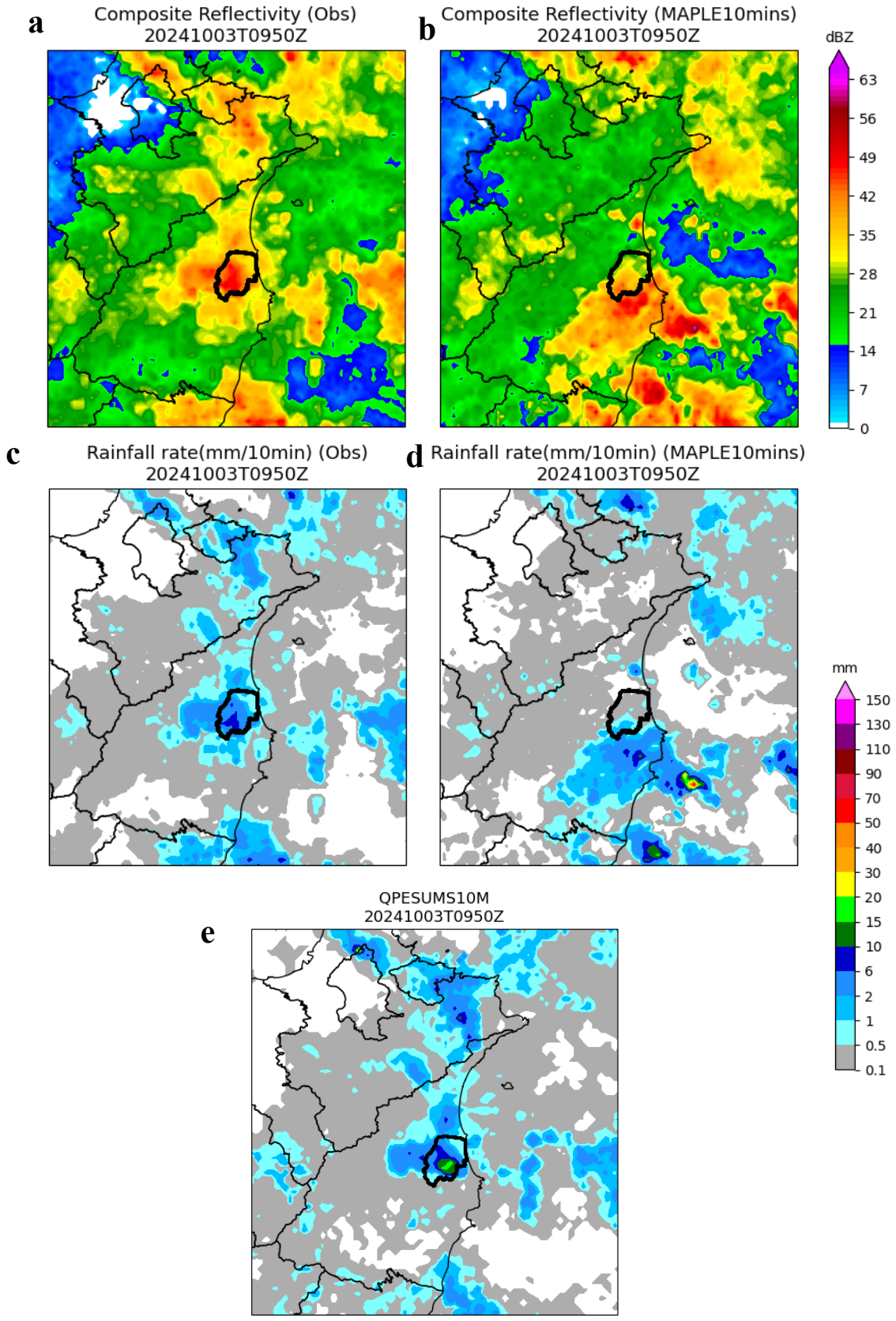

Figure 30. Observed and MAPLE forecast reflectivity, and convert to rainfall field by the Z-R relationship in the event 2024-10-03.

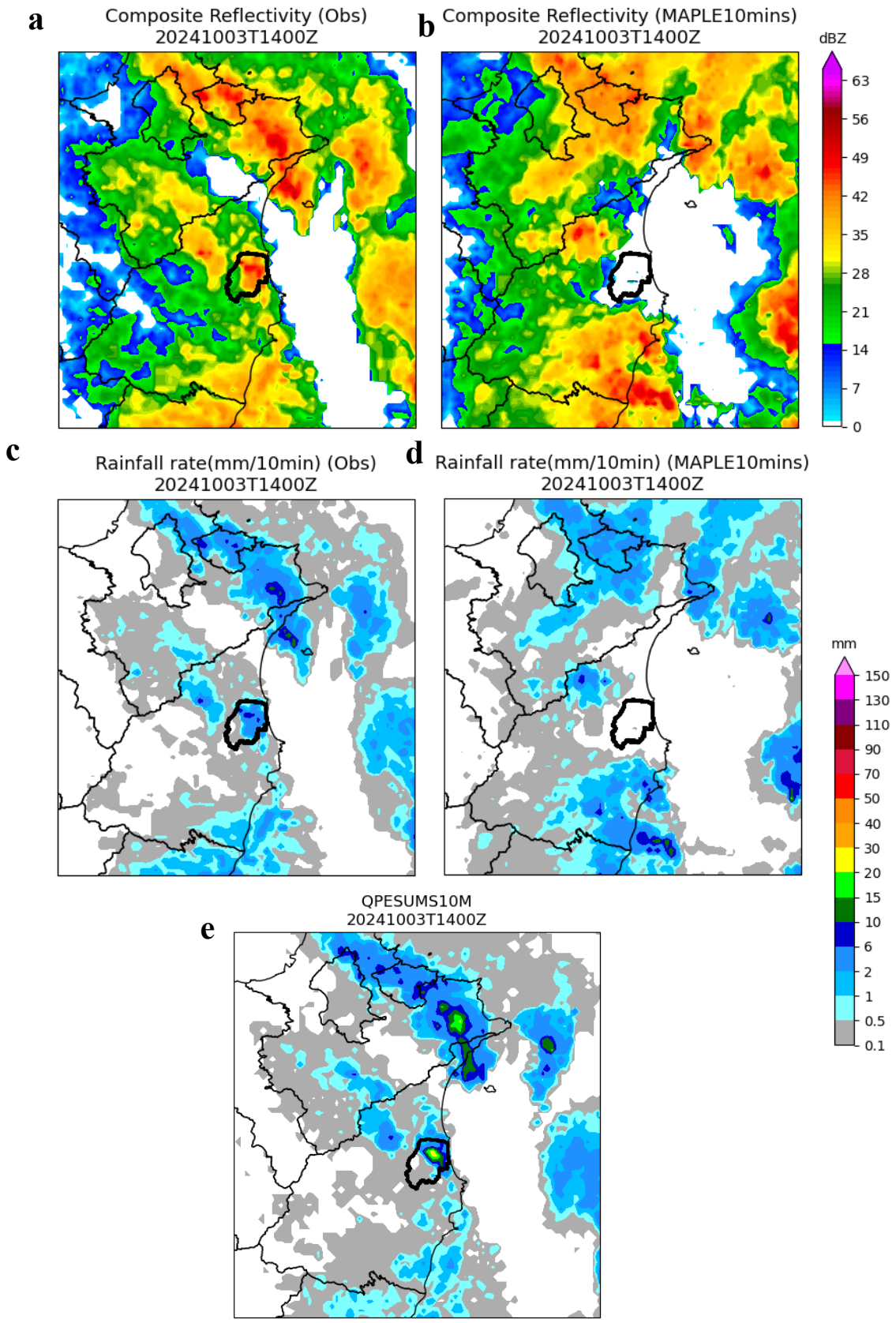

Figure 31. Observed and MAPLE forecast reflectivity, and convert to rainfall field by the Z-R relationship in the event 2024-10-03.

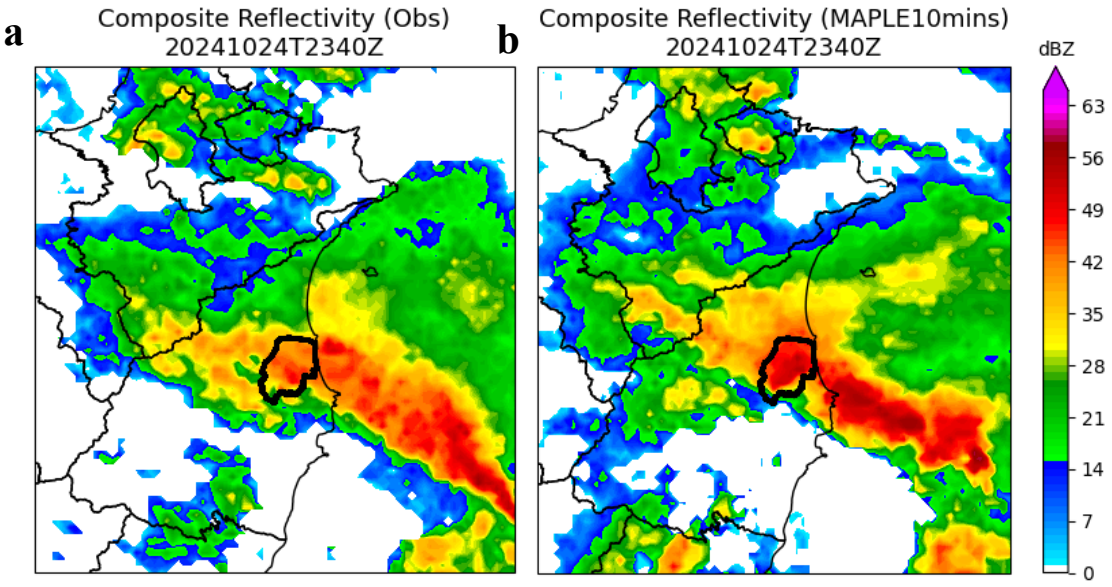

Figure 32. Observed and MAPLE forecast reflectivity in the event 2024-10-24.

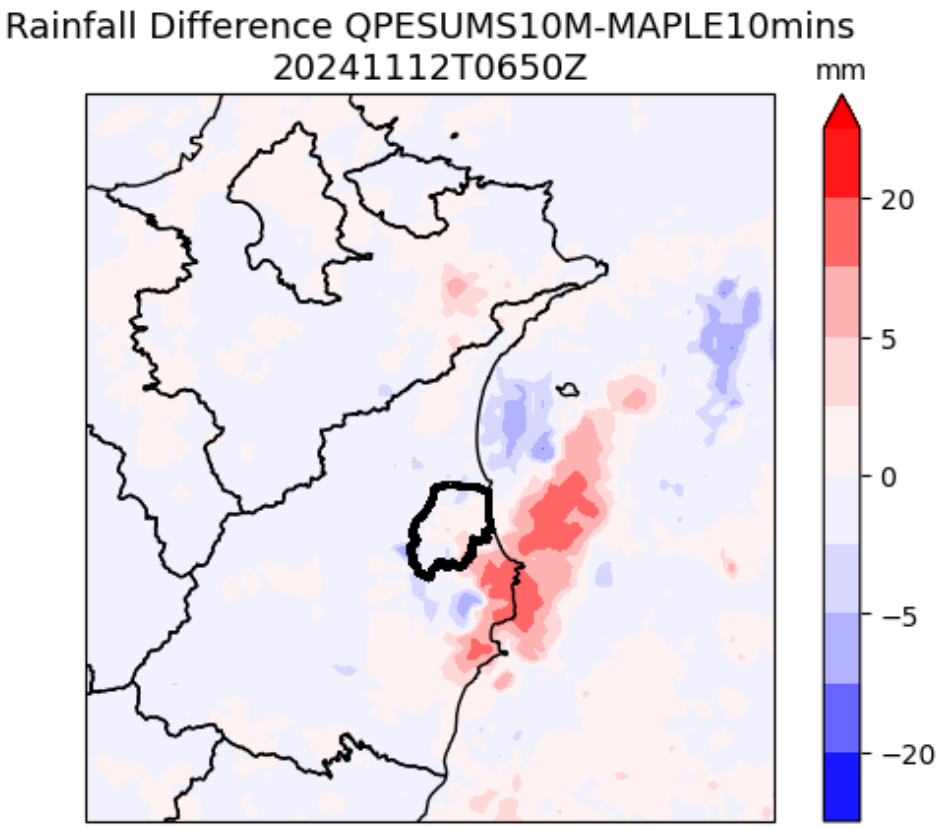

Figure 33. The difference between MAPLE10mins and QPESUMS10M.